THESIS FOR THE DEGREE OF LICENTIATE OF ENGINEERING

Corrosion of Ferritic Stainless Steels Used in Solid Oxide Fuel Cells

Evolution of Electrical Properties and Insights into the Dual Atmosphere Effect

Claudia Göbel

CHALMERS

Department of Chemistry and Chemical Engineering
CHALMERS UNIVERSITY OF TECHNOLOGY
Göteborg, Sweden 2018

Corrosion of Ferritic Stainless Steels Used in Solid Oxide Fuel Cells
Evolution of Electrical Properties and Insights into the Dual Atmosphere Effect
CLAUDIA GÖBEL

Licentiate Thesis at the Department of Chemistry and Chemical Engineering
Chalmers University of Technology
Nr: 2018:21
ISSN 1652-943X

Department of Chemistry and Chemical Engineering
Chalmers University of Technology
SE-412 96 Göteborg
Sweden
Telephone: +46 (0)31-772 1000

Cover:
Top: Dual atmosphere to which the ferritic stainless steel interconnects in a solid oxide fuel cell are subjected. *Bottom*: SEM micrographs of the air-facing side of AISI 441 exposed to dual atmosphere for 500 h at 600 °C. The samples were pre-oxidized prior to exposure for 180 min in air and, subsequently, the oxide layer on either the hydrogen-facing side (*right*) or the air-facing side (*left*) was removed by grinding the sample.

Chalmers Reproservice
Göteborg, Sweden 2018

Corrosion of Ferritic Stainless Steels Used in Solid Oxide Fuel Cells
Evolution of Electrical Properties and Insights into the Dual Atmosphere Effect
CLAUDIA GÖBEL
Department of Chemistry and Chemical Engineering
Chalmers University of Technology

Abstract

Solid oxide fuel cells (SOFC) are energy conversion systems with clean emissions (depending on the fuel used) and high electrical efficiencies, which could potentially replace conventional conversion systems such as combustion engines. However, other issues, such as high costs and limited lifetime, must be resolved before widespread commercialization of SOFCs can be achieved.

One of the major cost factors and the component that reduces the lifetime of SOFCs immensely, is the interconnect, which electrically connects multiple fuel cells to form a stack. Interconnects are typically made of ferritic stainless steels, and, due to high temperatures (600 °C - 900 °C) and the aggressive environments prevalent in fuel cells, the interconnects corrode over time. The protective Cr_2O_3 that forms on ferritic stainless steels at high temperatures mitigates the corrosion process to a certain extent. However, this oxide layer leads to two other issues: (i) vaporization of hexavalent Cr species, which leads to cathode poisoning and (ii) an increase in the electrical resistance of the interconnect caused by a continuously growing oxide layer. Both these problems can be reduced to a certain extent with coatings. Especially spinel coatings have been proven highly effective at decreasing Cr-evaporation.

The first part of this work examines the influence of the Co_3O_4 spinel coating on area specific resistance (ASR). It was found that the Co_3O_4 thickness of Crofer 22 APU, which was exposed in air for 500 h at 600 °C, did not significantly impact the ASR, and, instead, the main contributor to overall resistance was the thermally grown Cr_2O_3.

The second part of this work focuses on the long-term stability of Ce/Co-coated (10 nm Ce/640 nm Co) AISI 441. Coated AISI 441 was exposed by AB Sandvik Materials Technology for up to 37 000 hours at 800 °C in laboratory air. Subsequent analysis showed very low Cr-evaporation rates compared to uncoated AISI 441, and ASR values below 40 $m\Omega cm^2$, suggesting that, under these conditions, the coating is effective in reducing Cr-evaporation rates and Cr_2O_3-growth rates even after long exposure times.

The last part of the work analyzes the influence of pre-oxidation on the dual atmosphere effect at 600 °C with regard to two parameters: the pre-oxidation time and the pre-oxidation location. It was demonstrated that longer pre-oxidation times for AISI 441 result in extended resistance against dual atmosphere corrosion on the air-facing side. It was also found that the pre-oxidation layer on the hydrogen-facing side is more important for corrosion resistance in dual atmosphere than the pre-oxidation layer on the air-facing side.

Keywords: SOFC, Corrosion, Interconnect, Dual Atmosphere, Area Specific Resistance

Acknowledgements

I would like to take this opportunity to acknowledge all the people, who made this thesis possible.

First I would like to thank my main supervisor Associate Professor Jan Froitzheim and my co-supervisor Professor Jan-Erik Svensson for giving me the opportunity to complete my Licentiate in the Solid Oxide Fuel Cell Group at Chalmers University of Technology. I would like to thank you for all the guidance you provided me in the past 2.5 years and I am excited to learn even more in the coming years and have the chance to do more in-depth research with exciting new techniques under your supervision.

Of course the present work would not have been possible, without the help of the entire SOFC group. Thank you for welcoming me so warmly into the group and for teaching me how to work in the lab. Thank you to Ph.D. Patrik, for showing me how to build new dual atmosphere set-ups and for correcting my mistakes when I bent all the tubes wrong. Thanks to Maria for showing me how to do Cr-evaporation measurements and telling me that it is a moody system. And thank you, Ph.D. Hannes, for all the good discussions and for helping me with my interns. A big thanks goes also to all my interns and master thesis students, Robin, Alex, Matthieu, Maxime, Caterina and Thibault, who have helped me produce a ton of results. I would also like to acknowledge Mohammad Sattari, for showing me how the BIB works and all the rest of the SOFC staff that I have worked with or am going to work with in the near future: Ph.D. Christine, Ph.D. Vijay, Ph.D. Özgür and Reddy.

Special thanks also goes to Ph.D. Christine, who has always helped me order gas bottles or other stuff that I desperately needed for my private life, like a heat blanket. I would also like to thank Ph.D. Loli, Ph.D. Valentina and Andrea, who have helped me with all my questions regarding where I can find what, where to order what, and who to ask for what. Thank you to the entire high temperature corrosion center and the energy and materials division for all your help and for the warm welcome into this group. And special thanks to everyone, who joined for after-work beers or wine.

Thanks to the administrators, current or former, of our group Sandra, Susanne, Anna and Christina, for helping me out with all the administrative things and for managing to find places for all my interns.

Thanks to our industrial partners for providing us with interesting new research questions and good discussions. And a special thanks to AB Sandvik Materials Technology for sending us long-term exposed samples.

I wouldn't be here today, without the support of my family and friends. Therefore I want to thank my family, especially my parents Christine and Karl Göbel. Without their continuous support I would have never gotten this far. Thank you so much! And last but not least I want to thank Hannes for supporting me and urging me on in the last few months and for answering all my work related questions even when he was tired!

List of Publications

This thesis is based on the following papers:

I C. Göbel, A. G. Fefekos, J.-E. Svensson and J. Froitzheim. Does the conductivity of interconnect coatings matter for solid oxide fuel cell applications? *Journal of Power Sources* **383** (2018), 110-114.

II C. Göbel, R. Berger, M.W. Lundberg, J. Westlinder, J.-E. Svensson and J. Froitzheim. Long Term (4 Years) Performance of Co/Ce Coated 441 for SOFC Interconnect Applications. *ECS Transactions* **78** (2017), 1675-1679.

III C. Göbel, P. Alnegren, R.L. Faust, J.-E. Svensson and J. Froitzheim. The effect of pre-oxidation parameters on the corrosion behavior of AISI 441 in dual atmosphere. *International Journal of Hydrogen Energy* **43** (2018), 14665-14674.

Statement of author's contribution

I was the main author of all the appended papers. The resistance measurements and the x-ray diffraction analysis in Paper I were done mainly by Alexander G. Fefekos within the scope of an internship under my supervision. I carried out the microstructural analysis using scanning electron microscopy. Sandvik Materials Technology exposed some of the samples for up to 37 000 h for Paper II, and I did the subsequent analysis of these samples, e.g. Cr evaporation measurements, resistance measurements, and microstructural investigations. Most of the experimental work in Paper III was conducted by Robin Faust within the scope of his master thesis under my supervision.

Related Work

The following paper is directly related to the work discussed in this thesis:

C. Göbel, P. Alnegren, R.L. Faust, J.-E. Svensson and J. Froitzheim. Influence of Pre-Oxidation on Dual Atmosphere Effect on AISI 441 Interconnects for Solid Oxide Fuel Cell Applications. *ECS Transactions* **78** (2017), 1559-1563.

List of Acronyms

APU	Auxiliary Power Unit
ASR	Area Specific Resistance
BCC	Body-Centered Cubic
BSE	Backscattered Electron
CGO	Gadolina-Doped Ceria
CHP	Combined Heat and Power
EDX	Energy Dispersive X-ray
FC	Fuel Cell
FCC	Face-Centered Cubic
FSS	Ferritic Stainless Steel
GDOES	Glow-Discharge Optical Emission Spectroscopy
InCF	Intrinsic Chemical Failure
IT	Intermediate Temperature
LSM	Sr-doped $LaMnO_3$
MCO	$(Mn,Co)_3O_4$
MICF	Mechanically Induced Chemical Failure
MIEC	Mixed Ionic and Electronic Conductors
PBR	Pilling and Bedworth Ratio
PVD	Physical Vapor Deposition
RE	Reactive Elements
SEM	Scanning Electron Microscopy
SMT	Sandvik Materials Technology
SOFC	Solid Oxide Fuel Cell
TEC	Thermal Expansion Coefficient
TPB	Triple-Phase-Boundary
XRD	X-Ray Diffraction
YSZ	Yttria Stabilized Zirconia

Contents

Chapter 1

Introduction

1.1 Background

The human contribution to climate change has been well-established for many decades, and attempts to reduce these anthropogenic contributions rely heavily on advanced renewable energy generation systems [1]. Some of these new systems, such as wind and solar power, have the drawback that they are intermittent, therefore, energy storage technologies are becoming more and more important and, with that, also flexible and green energy conversion systems are needed [2]. The applications for energy systems are plentiful not only for grid scale storage but also for mobile applications in transport and portable devices, or for stationary applications such as power supply for housing and factories. Besides combined energy storage and conversion systems, such as secondary batteries, energy can also be stored in fuels, such as hydrogen, and, when needed, the chemical energy can be converted into electrical energy by conversion systems such as fuel cells. The differences between each energy conversion technology result in different advantages and disadvantages of each technology. For example, secondary batteries are combined energy storage and conversion systems, however, they require regular recharging, in contrast, fuel cells can provide constant electrical energy if a continuous fuel supply is provided [3]. The different advantages of each system and the need for more than one functioning technology lead to research being conducted simultaneously on batteries and fuel cells and other alternative systems.

A fuel, primarily hydrogen, is used in the fuel cell system as an energy carrier, and, during fuel cell operation, the oxidation of hydrogen and formation of H_2O occurs. For most fuel cell types, for example the proton exchange membrane (PEM), only hydrogen with very high purity can be used as the fuel. This limitation greatly impacts the applicability of the technology for some uses. Therefore, fuel cells with greater fuel flexibility, such as the solid oxide fuel cell (SOFC), are an interesting alternative. To achieve this flexibility, a solid oxide, which conducts oxygen ions, is used as the electrolyte instead of, for example, a proton exchange membrane. On the other hand, one drawback of the SOFC system is the rather high operating temperature, which ranges between 600 °C and 900 °C compared to the low operating temperatures of around 80 °C in PEM fuel cells. However, this additional heat can be used in combined heat and power (CHP) units or for further energy generation with steam turbines. The re-utilization of the waste heat can increase the already high electrical efficiency of a fuel cell (above 60 %) and overall system efficiencies of up to 90 % can be achieved [4–7].

The bipolar plates or interconnects are an integral part of any fuel cell system. These connect multiple fuel cells in series to form a fuel cell stack with reasonable voltage outputs. The interconnects for SOFCs are nowadays typically made of ferritic stainless steels (FSS), and the interconnects account for nearly 35 % of the overall cost for a 1 kW stack with a production volume of 50 000 units [8]. As cost is one of the major issues to overcome before widespread commercialization of SOFCs can be achieved, research that focuses on interconnects and how to reduce the cost of these is important [7, 9, 10].

Another issue of the SOFC system besides the high cost is limited lifetime. A lifetime of at least 40 000 h for stationary applications is necessary for successful commercialization. The main reason for the limited lifetime of a fuel cell is material degradation mainly due to the high operating temperatures above 600 °C. Metallic interconnects, in particular, suffer under these conditions, and corrosion phenomena, such as increased electrical resistance, Cr evaporation, and the dual atmosphere effect, impact the lifetime of the fuel cell dramatically [10, 11].

Additional understanding of the corrosion processes occurring on the interconnect level can result in mitigation strategies. For example, Cr evaporation can be decreased significantly by coatings, such as $(Mn,Co)_3O_4$, and, thus, Cr depletion of the material and Cr poisoning of the cathode can be avoided [12–14]. In addition, some coatings, such as Ce coatings, decrease the growth rate of the oxide scale that forms on an interconnect at high temperatures, which results in longer lifetimes because less Cr is consumed [15, 16]. Reduced oxide scale growth also leads to lower resistances, as the main contributors to the overall resistance of an interconnect are the oxide scales. Therefore, today, the general consensus is that coatings on an interconnect greatly increase fuel cell lifetime.

Corrosion phenomena must be mechanistically understood before highly efficient mitigation strategies can be developed. These phenomena include the dual atmosphere effect, i.e. increased corrosion on the air-facing side if the FSS is simultaneously exposed to air on one side and hydrogen on the other side, compared to FSS that is only exposed to air atmosphere [17].

Research is needed to understand the corrosion processes on the interconnect level in a SOFC and solutions that are not only cost-efficient but also lifetime prolonging must be found. Only then will widespread commercialization of SOFC be successful.

1.2 Aim of this Thesis

The present work deals with different corrosion mechanisms that occur on the interconnect level in a solid oxide fuel cell.

The first part focuses on coatings used for the interconnect application. Coatings are applied to interconnects to mitigate Cr-evaporation and to decrease the oxide scale growth [10, 11]. Especially spinel coatings are commonly used, because of their good Cr retention rates [12–14]. However, adding additional oxide coatings to an interconnect could potentially increase the electrical resistance of an interconnect. Therefore, researchers are trying to increase the conductivity of the coatings by adding dopants [11, 18]. Besides, the coating, however, also the continuously growing Cr_2O_3 could increase the electrical resistance even further. The present work discusses if the main contributor to the electrical

resistance is the coating or the Cr_2O_3. In the latter case efforts to increase the coating conductivity might not be effective in decreasing the overall resistance of the interconnect and instead research should focus on decreasing the Cr_2O_3 scale growth. To analyze this, Crofer 22 APU was coated with different Co coating thicknesses, and, after a 500 h exposure at 600 °C, the area specific resistance (ASR) was measured. An influence of Co coating thickness on the ASR should be seen if the coating greatly influences the overall resistance.

To further understand the longevity of the state-of-the-art interconnect coating, Ce/Co-coated (10 nm Ce and 640 nm Co) AISI 441 was also examined in the present thesis[19]. For this purpose, the material was exposed by AB Sandvik Materials Technology up to 37 000 h at 800 °C in air. After exposure, Cr evaporation, electrical resistance, and microstructural analysis were conducted on the material.

The second part of this work deals with the influence of the atmosphere present inside the fuel cell on material degradation. As mentioned in Chapter 1.1, in a SOFC, interconnects are exposed to a dual atmosphere, and, because of this, corrosion was found to increase especially at temperatures around 600 °C [20, 21]. This so called dual atmosphere effect is not yet mechanistically understood. This work discusses the dual atmosphere effect, especially with regard to a pre-oxidation step in air implemented before dual atmosphere exposure.

Chapter 2

Theory

2.1 Fuel Cells

2.1.1 Introduction to Fuel Cells

Fuel cells efficiently generate electricity by converting chemical energy into electrical energy. The working principle of the fuel cell was discovered independently by William Grove and Christian Friedrich Schönbein in 1838 [22]. Both discussed a crude and simple setup, which, nonetheless, was able to convert the chemical energy set free during the formation of H_2O from hydrogen and oxygen to electrical energy [23].

Fuel cells function similar to batteries; a chemical redox reaction is locally separated into oxidation and reduction reactions, thus avoiding combustion, and converting the chemical energy safely to electrical energy. The overall reaction equation for most fuel cells is shown in Equation 2.1.

$$\frac{1}{2}O_2 + H_2 \longrightarrow H_2O \tag{2.1}$$

To separate reaction into oxidation and reduction, an electrolyte is inserted between the cathode, where the reduction takes place, and the anode, where the oxidation takes place. The most important requirements for any electrolyte material are high ionic conductivity but very low electronic conductivity. The latter property ensures that the electrons are conducted through an external circuit [9].

Different classifications of fuel cell types typically involve the electrolyte material, as this defines not only the operating temperature of the fuel cell but also which ions are conducted and what fuels can be used for the fuel cell. For example, the Polymer Exchange Membrane Fuel Cell (PEM-FC) conducts protons, and, because of that, only high purity H_2 with no CO contaminants can be used as a fuel. Operating temperatures for this fuel cell type range between 70 and 110 °C [9, 23]. In contrast, fuel cells with an oxide conductor as the electrolyte, such as Solid Oxide Fuel Cells (SOFC) have high fuel flexibility, and, thus, besides hydrogen, simple hydrocarbon compounds, such as ethanol or methanol and even complex hydrocarbons like diesel reformate, can be used as fuels [7]. Therefore, one of the big advantages of SOFCs is that no new infrastructure is required. The biggest drawbacks of the SOFC system, however, are the high cost and the necessity for high operating temperatures above 600 °C. The high temperature leads to slower start-up times than the PEM-FC and increased material degradation of certain

components in the fuel cell [7]. In part due to the difference in start-up time, the possible applications for both techniques, PEM-FC and SOFC, differ. While PEM-FCs are mostly being considered for mobile applications and transportation purposes, SOFCs are mostly being considered as auxiliary power units (APU) in trucks, range-extenders in cars, or for stationary applications, such as combined heat and power (CHP) units in housing [9].

The high operating temperature of a SOFC is not only a disadvantage, but it can also be an advantage. For example, the high operating temperature nullifies the need for expensive Pt-catalysts that are needed at lower temperatures, and the heat can be used in said CHP units for housing [24, 25]. Another advantage SOFCs have over PEM-FCs is their high efficiencies. With electrical efficiencies of above 60 %, [5] (compared to up to 50 % for PEM-FC [26]) and possible overall efficiencies of above 90 % for systems that use exhaust heat for heating in CHP units or for further electricity generation using heat engines or steam turbines, the SOFC system is promising as a future technology [4, 5, 25, 27]. However, to achieve widespread commercialization of this technology, the high cost of the SOFC must be positively influenced, and, hopefully, the further development of the technology will eventually allow for cheaper materials to be used. The solid oxide fuel cell will be discussed in more detail in the following.

2.1.2 Solid Oxide Fuel Cell

As mentioned in chapter 1.1 the electrolyte in a SOFC is a solid oxide, and an oxygen ion conductor. This allows for the fuel flexibility of the system, but, in turn, high temperatures are required to ensure oxygen conductivity. If H_2 is used as the fuel, the following reaction processes happen inside the fuel cell:

$$Oxidation: \quad H_2 + O^{2-} \longrightarrow H_2O + 2e^- \tag{2.2}$$

$$Reduction: \quad \frac{1}{2}O_2 + 2e^- \longrightarrow O^{2-} \tag{2.3}$$

$$Overall\ Reaction: \quad \frac{1}{2}O_2 + H_2 \longrightarrow H_2O \tag{2.4}$$

While the oxidation of hydrogen happens at the anode, the reduction of oxygen takes place at the cathode of the fuel cell. These processes, including the oxygen ion diffusion through the electrolyte and the electron transfer through an external circuit, are visualized in Figure 2.1a.

Because of thermodynamic limitations, the energy output of one fuel cell is below 1.2 V [9, 28], therefore, multiple cells must be electrically connected in series with so called interconnects to form a fuel cell stack (see Figure 2.1b). Information on the different materials used for the electrodes, the electrolyte, and the interconnect and what requirement each component must fulfil are provided in the following. Due to the high operating temperatures, all materials used in the fuel cell stack should have similar thermal expansion coefficients (TEC), otherwise thermal stresses could occur during start-up or shut-down.

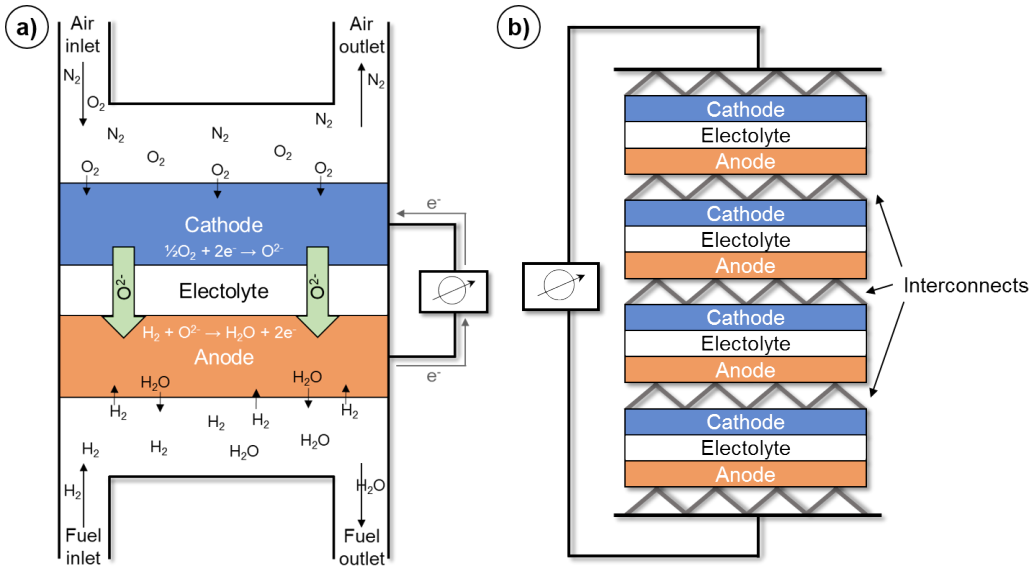

Figure 2.1: *Solid oxide fuel cell. a) Operating principle and b) Fuel cell stack.*

Electrolyte The electrolyte must be stable at high temperatures. As it separates the anode from the cathode it must also be stable in reducing and oxidizing atmospheres, and it must be non-porous and dense to be able to separate the fuel and the air from each other. While the electrolyte must be oxygen-ion conductive, it must be a poor electron conductor because the electrons must be transferred through the external circuit [29]. Popular choices for electrolyte materials are yttria-stabilized zirconia (YSZ) for high operating temperatures above 700 °C and gadolina-doped ceria (CGO) for lower temperatures [30–32].

Anode Anode materials must also be stable at high temperatures and in reducing atmospheres. The material also needs to be catalytically active for the fuel oxidation. The anode material must be porous to ensure a sufficiently large catalytically active surface area and to allow for easy gas flow and removal of the half reaction products (see Equation 2.2) from the electrode. Other requirements that must be met are high oxygen ion and electron conductivity to ensure good transportation of ions and electrons to the electrolyte or the external circuit, respectively [33]. The anode material is often a mixture between the electrolyte material, which leads to a good TEC match between anode and electrolyte, and another material with high electron conductivity, which also ensures pore formation [33, 34]. A commonly used anode material, for example, is Ni-YSZ [35].

Cathode Cathode materials must also be stable at high temperatures, but, in contrast to the anode material, the cathode material must be stable in oxidizing atmospheres and be catalytically active for oxygen reduction. Similar to the anode, the cathode also requires high electron conductivity and high porosity to ensure a large catalytically

active surface area, good gas flow, and extraction of the products of the half-reaction, Equation 2.3 [36]. Today, solid oxides are typically used as cathode materials because other options, such as precious metals, are very expensive. A commonly used cathode material is Sr-doped $LaMnO_3$ (LSM). One limitation for LSM is its very poor oxygen ion conductivity, which leads to a small triple-phase-boundary (TPB) area. To increase this area YSZ is sometimes added to LSM, which leads to a higher oxygen ion conductivity [37, 38]. Especially for intermediate temperature SOFCs (IT SOFC), mixed ionic and electronic conductors (MIEC) are preferred, and a commonly found cathode material in IT SOFCs is $(La,Sr)(Co,Fe)O_3$ (LSCF)[24, 39].

Interconnects Like the electrolyte, the interconnect must be stable at high temperatures and in oxidizing and reducing atmospheres as the interconnect also separates fuel and air from each other. Therefore, the interconnect must be non-permeable to both gases. An additional function of the interconnect is the distribution of the gases throughout the electrode surface. However, the primary function of the interconnect is to electrically connect multiple fuel cells in series, and, therefore, it must be, contrary to the electrolyte, an electron conductor. Hence, the interconnect acts as a current collector [40]. Other requirements sought for materials used as interconnects are high thermal conductivity, ease of formability, and cheap to produce.

Previously, mainly ceramics were used as interconnects, especially perovskites, such as $LaCrO_3$ doped with Ca or Sr. These oxides are semiconductors and, therefore, require high temperatures around or above 1000 °C to be sufficiently electron conducting. They are also not cost-effective or easily formable. However, with further developments of the electrode and electrolyte materials, a decrease in operating temperatures to below 850 °C was possible. This has warranted a search for new interconnect materials, and, nowadays, metallic interconnects are the standard for SOFCs with operating temperatures below 850 °C [10, 41, 42].

While metallic interconnects show many promising properties, such as much lower costs than ceramic interconnects, ease of formability, and high electrical and thermal conductivities, the long-term stability of the material at high temperatures in aggressive environments remains an issue. The most commonly used metals are ferritic stainless steels (FSS) with more than 16 % Cr content. This steel typically forms a thin Cr_2O_3 on top of the metal. This so-called protective oxide layer has the advantage of slowing down any corrosion occurring on the metal, while at the same time it has the disadvantage of increasing the electrical resistance of the interconnect, as Cr_2O_3 is a semi-conductor.

The scope of the present work is the examination of the degradation behavior of metallic interconnects at temperatures between 600 °C and 800 °C and the analysis of possible solutions to this problem. More insight into the oxidation of metals is given below, to understand the corrosion phenomena occurring at the interconnect level of a fuel cell. This theory will then be put into context with the corrosion behavior of interconnects in the fuel cell environment.

2.2 Oxidation of Metals

Most metals are not thermodynamically stable under ambient pressure, instead the oxidation products, such as oxides, sulphides, or nitrides, are stable under these conditions. The focus of this work is on oxide formation and the following reaction (Reaction 2.5) that occurs during oxidation of the metal:

$$xM(s) + \frac{y}{2}O_2(g) \longrightarrow M_xO_y(s) \tag{2.5}$$

However, even though the oxidized metal is the thermodynamically stable form, the kinetics of Reaction 2.5 at ambient temperature is often not favorable. A different picture emerges at higher temperatures [43]. To further explain the processes happening at high temperatures, some information is given on the thermodynamics of Reaction 2.5 and the kinetics of said reaction and how these factors influence the oxidation behavior of a metal. This will be followed by an explanation of oxide scale growth, and evaporation phenomena will be briefly discussed.

2.2.1 Thermodynamics

To determine if the metal or the oxide is stable under certain conditions, the Gibbs energy of a systems can be calculated (see Equation 2.6).

$$G = H - TS, \tag{2.6}$$

where G is the Gibbs energy, H is the enthalpy, T is the temperature, and S is the entropy. This energy is derived from the second law of thermodynamics with the assumption that the temperature and the pressure of the system are constant. For systems with $\Delta G < 0$, Reaction 2.5 will occur spontaneously, systems with $\Delta G = 0$ are in equilibrium state, and for systems with $\Delta G > 0$, Reaction 2.5 is thermodynamically impossible [15, 43]. The ΔG for Reaction 2.5 per mole oxygen can be expressed as Equation 2.7.

$$\Delta G = \Delta G^0 + RT \ln \left(\frac{a_{M_xOy}^{2/y}}{a_M^{2x/y} a_{O_2}} \right), \tag{2.7}$$

where ΔG^0 is the change in standard free energy for the formation of M_xO_y, R is the gas constant, T is the absolute temperature, and a_z is the thermodynamic activity of a species z. In general, the activity of solids can be assumed as 1, and the activity of gases is approximated to the partial pressure of said gas, i.e. $a_{O_2} = p_{O_2}$. Therefore, the following equation (Equation 2.8) is valid for the equilibrium state $\Delta G = 0$ of Equation 2.7.

$$\Delta G^0 = RT \ln p_{O_2}. \tag{2.8}$$

According to Equation 2.8, two factors are important to determine whether a metal

oxide or the metal is stable under certain conditions: the temperature T and the partial oxygen pressure p_{O_2}. Ellingham/Richardson diagrams are a useful tool to visualize this for many different oxides (see Figure 2.2) [44]. These diagrams exist not only for oxides, but also for other oxidized metals species, such as sulphides or nitrides. The equilibrium state of different metal oxides is depicted in the Ellingham diagram. The metal oxides with lower ΔG are more stable than the metal oxides with a higher ΔG, making Al_2O_3 the most stable oxide depicted in Figure 2.2 [43].

2.2.2 Kinetics

In addition to the briefly discussed thermodynamics the kinetics of Reaction 2.5 also play a role in high temperature corrosion. Kinetics is important to understand the reaction mechanism and to determine the rate-limiting step of a reaction. To analyze the rate of Reaction 2.5, three different aspects can be examined: how much metal was consumed, how much oxygen was consumed, or how much oxide was formed. Of these options, the latter one is the method that is most used today as it is experimentally most accessible (measure the weight gain of the sample), and the measurement can be done continuously throughout the reaction [15].

Different rate laws can be formulated for a kinetic evaluation of a reaction. The three most commonly found rate laws for metal oxidation are the linear, logarithmic, and parabolic rate laws, which are visualized in Figure 2.3 as mass gain against time. However, many reactions do not follow these ideal cases and deviations or even mixtures of the different rate laws are common. Nevertheless, the rate laws can give some insight into the classification of an oxide, and also help in deciding if an oxide is more or less protective [43].

Linear Rate Equation The linear rate law is given by the following Equation 2.9:

$$x = k_l t + C, \tag{2.9}$$

where x is the oxide thickness and can be substituted with the mass gain Δm, k_l is the linear rate constant, and C is the integration constant. No decrease in mass gain is observed over time for oxide formations that follow this rate law. The rate-determining step for this reaction behavior is usually either a phase-boundary or a surface process, such as oxygen adsorption onto the metal surface. The behavior is mostly found for very thin oxides or very porous oxides [43].

Logarithmic Rate Equations At intermediate temperatures around 300 to 400 °C and for very thin metal oxide scales of up to 4 nm [15], the metal-oxide formation often follows a logarithmic rate law. Two different commonly seen logarithmic laws are given in Equations 2.10 and 2.11 [15].

$$\textit{Direct Logarithmic} : x = k_{\log} \log(t + t_0) + A, \tag{2.10}$$

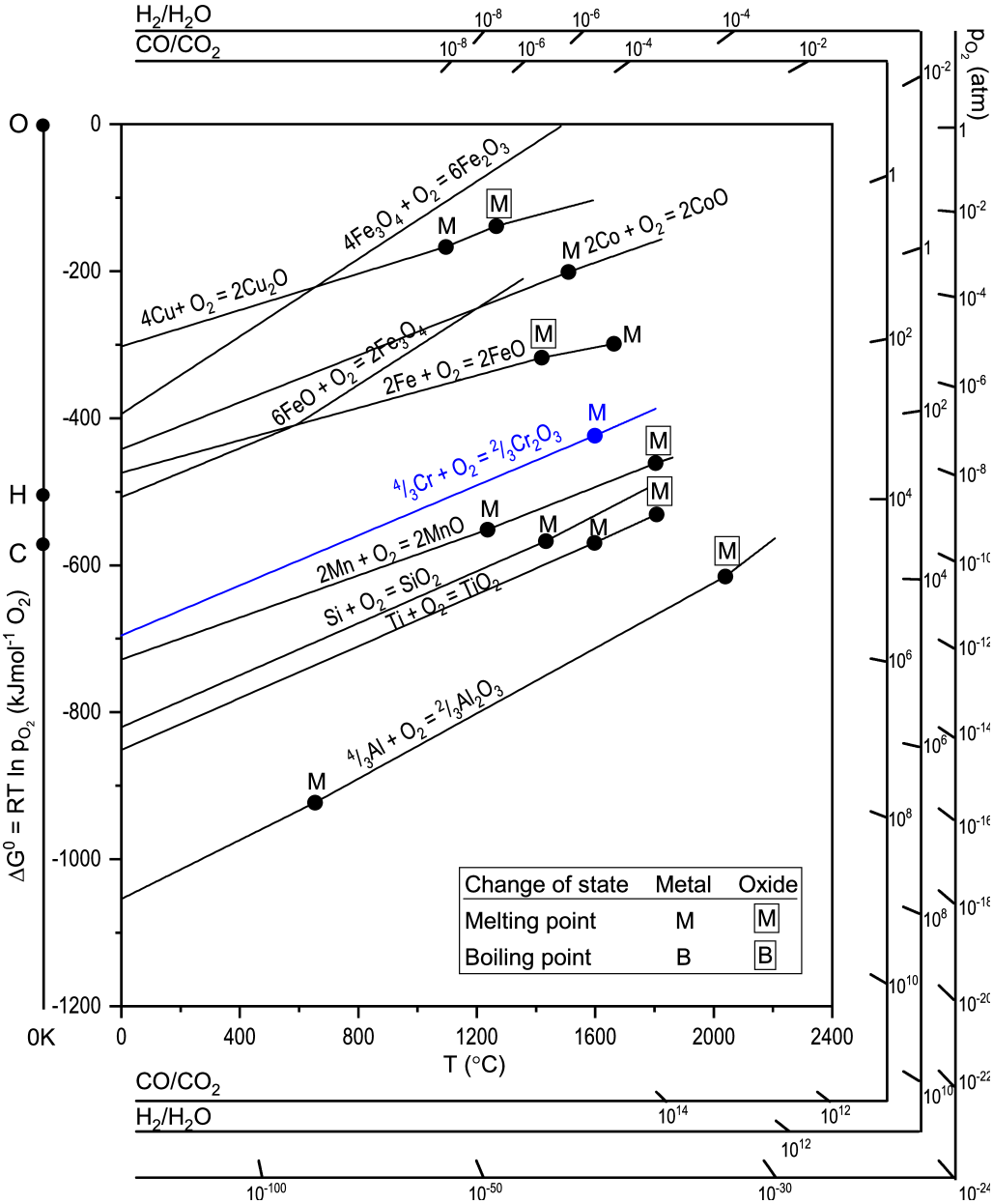

Figure 2.2: *Elingham Diagram for selected oxides based on [43, 45].*

$$Inverse\,Logarithmic: \frac{1}{x} = B - k_{il} \log t, \tag{2.11}$$

where x is the oxide thickness or the mass gain Δm, k_{log} is the logarithmic, and k_{il} the

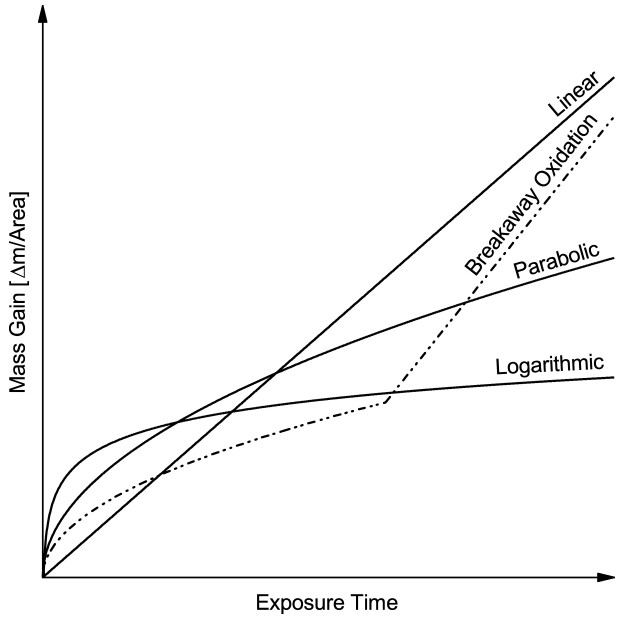

Figure 2.3: *Typical growth behavior of metal oxides [43].*

inverse logarithmic rate constant, t is the exposure time, and A and B are the integration constants. The rate-determining step for these rate laws is not yet fully understood and suggestions, such as the transport of ions or electrons through the oxide scale with an existing electric field through the scale or chemisorption, have been proposed [43].

Parabolic Rate Equation The oxidation of metals at high temperatures often follows the parabolic rate law (see Equation 2.12).

$$x^2 = k_p t + C, \tag{2.12}$$

where x is the oxide thickness or the mass gain Δm, k_p is the parabolic rate constant, t is the exposure time, and C is the integration constant.

Further description of oxides that follow the parabolic rate law was given by Carl Wagner in 1933 [46], who developed a theory for parabolically growing oxides, which is based on following assumptions [15]:

- The formed oxide scale is dense and well-adherent.
- The rate-determining step is solid-state diffusion of ions and electrons through the scale.
- Both interfaces, the metal-oxide and the oxide-gas, are in a thermodynamic equilibrium state.
- The stoichiometry of the oxide is near constant throughout the scale.

- The scale is in thermodynamic equilibrium throughout the scale.
- The thickness of the scale is much greater than the maximum length where charge effects occur.
- Oxygen solubility is negligible in the metal.

In general, metal oxides that follow the parabolic rate law grow slower with time due to a thicker oxide scale, and therefore longer diffusion paths. The resulting oxide scales are often described as protective oxide scales.

Breakaway Oxidation As mentioned in Chapter 2.2.2, in reality, the oxide scale growth often follows a mixture of different rate laws, or the reaction behavior changes for different reasons, such as the achievement of a critical oxide scale thickness, the formation of cracks due to stresses, or the depletion of an alloying element. One frequently seen mixture of rate laws is breakaway oxidation (see Figure 2.3). Breakaway oxidation is usually found for oxide scales that follow the parabolic rate law until they reach a critical point, after which the mass gain suddenly increases linearly. Only after the switch from parabolic to linear mass gain is the term breakaway oxidation used [43, 47].

Different reasons for breakaway oxidation exist. The most common ones are either due to mechanically induced chemical failure (MICF) or intrinsic chemical failure (InCF) [47]. In the case of MICF the oxide scale reaches a critical thickness and cracks, ruptures, or even experiences spallation. This leads to direct contact between the gas and the alloy and three different cases can then be observed:

- Continuous protective behavior occurs if the protective oxide forming element, e.g. Al or Cr, is not depleted in the underlying alloy and further crack and rupture formation is below a critical value [43, 47].
- Non-protective behavior occurs if the underlying alloy is locally depleted of the protective oxide-forming element, e.g. Al or Cr, and instead non-protective, fast-growing Fe-rich oxide forms [48].
- Non-protective behavior can occur even though the underlying alloy is not depleted of the protective forming oxide if the formed cracks and ruptures nucleate and propagate continuously [43].

In the case of InCF the element forming the protective oxide scale is depleted (e.g. Cr) at the oxide metal interface. The formation of the protective oxide then becomes thermodynamically less favorable, and, instead, the formation of a non- or less protective fast-growing metal-oxide (e.g. Fe-rich oxide) scale may occur [43, 47].

The formation of breakaway oxidation can be influenced by outside factors. For example, it is generally acknowledged that for Cr_2O_3-forming alloys, the presence of water vapor in high pO_2 atmospheres greatly increases the risk of the formation of breakaway oxidation [49–51]. One of the reasons for this is Cr evaporation, which will be discussed in more detail in Chapter 2.2.4. In low pO_2 environments, the presence of water vapor can also lead to a change in oxidation behavior. However, in these environments breakaway oxidation is only found in rare cases [52, 53].

2.2.3 Oxide Scale Growth

Oxide scale growth is a three-step process that is visualized in Figure 2.4. First, oxygen is adsorbed onto the metal surface. Then a metal oxide is formed as a nuclei on the metal-air interface, and, in the last step, the scale grows continuously. The first two steps of the oxide scale growth are mainly dependent on surface conditions, such as surface preparation or surface defects, and gas or metal impurities. However, the third step is solid-state diffusion-dependent, because either the metal cations must diffuse to the oxide-air interface or the oxygen anions must diffuse to the metal-oxide interface [43]. Protective oxide scales, such as Cr_2O_3, are distinguished by their low density, porosity, and ion diffusivity, the latter leading to a slow-growing oxide scale. At high temperatures, the third step is typically the rate-determining step [15].

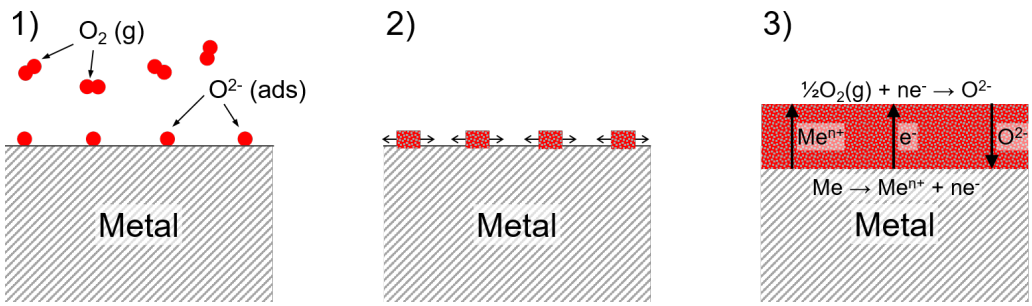

Figure 2.4: *Schematic drawing of the process of oxide growth on a metal substrate according to [43]. The three main steps are: 1) Oxygen adsorption, 2) Oxide nucleation, and 3) continuous oxide scale growth.*

Pilling-Bedworth Ratio A way to classify oxides as either protective or non-protective was suggested by N. B. Pilling and R. E. Bedworth in 1923 [54]. They stated that the volume ratio of the metal oxide versus the metal itself relates to the protective property of the oxide (see Equation 2.13), as this ratio defines what stresses are prevalent in the oxide [15, 43].

$$PBR = \frac{V_{oxide}}{V_{metal}}. \tag{2.13}$$

Tensile stresses should be present for PBR values below 1, whereas compressive stresses are present for PBR values greater than 1. Additionally, PBR ratios below 1 could result in a porous oxide that does not cover the entire metal surface, which is an important factor for the protectiveness of an oxide scale. This led Pilling and Bedworth to believe that PBR values greater than one will result in the formation of a protective oxide. Their assumption was based on an inward-growing oxide, meaning that the oxide grows on the metal-oxide interface, and oxygen inward diffusion is the predominant diffusion. However, today, we know that there are many exceptions to this rule, and, therefore, the

classification of an oxide into protectiveness and non-protectiveness is not straight-forward [15, 43]. Nevertheless, the Pilling and Bedworth ratio (PBR) can still be used, and it is used in the present work to define the volume increase that occurs when a metal is oxidized to the metal oxide. Some important PBR values are given in Table 2.1.

Table 2.1: PBR values for some metal-oxygen systems. Unless otherwise stated, the values were taken from [15].

Oxide	PBR
Al_2O_3	1.28
Cu_2O	1.64
FeO (on α-Fe)	1.68
CoO	1.86
Co_3O_4	1.98 [55]
Cr_2O_3	2.07
Fe_3O_4 (on α-Fe)	2.10
Fe_2O_3 (on α-Fe)	2.14

2.2.4 Oxide Evaporation

A corrosion-related phenomenon that different alloying elements, such as Cr, Mn and W, are subject to, is the evaporation of certain volatile metal oxide species. This evaporation process has typically a rather high activation energy, therefore, the process becomes especially relevant at high temperatures [43]. The focus in the following will be on Cr evaporation, as this mechanism is relevant to the present work.

Cr-containing alloys form a protective, slow growing, and dense Cr_2O_3 layer. However, under certain conditions, other gaseous Cr species may form, such as CrO_3. The formation of CrO_3 (Equation 2.14) requires high temperatures and high oxygen pressures (approximately $T = 1\,000\,°C$ and $p_{O_2} = 1$ atm [43]) to be of significance for the lifetime of an alloy. However, another volatile Cr-species, $CrO_2(OH)_2$, will form (see Equation 2.15) at much lower temperatures in the presence of water vapor. This is in agreement with the difference in activation energies of the two hexavalent Cr species. While the formation of CrO_3 has a high activation energy and is, therefore, highly dependent on temperature, the formation of $CrO_2(OH)_2$ has a much lower activation energy and is, thus, much less temperature dependent [56].

$$Cr_2O_3(s) + \frac{3}{2}O_2(g) \longrightarrow 2CrO_3(g) \tag{2.14}$$

$$Cr_2O_3(s) + 2H_2O(g) + \frac{3}{2}O_2(g) \longrightarrow 2CrO_2(OH)_2(g) \tag{2.15}$$

Different research groups have found that the main volatile species present is $CrO_2(OH)_2$ even with only small amounts of water vapor presen [56–58].

The Cr consumption of a system in which the volatilization of hexavalent Cr species occurs, increases because two parallel processes consummate the Cr: the Cr-evaporation process, and the continuous growth of the Cr_2O_3 scale. Most systems will eventually reach a steady-state scale thickness, which is expressed as a weight loss in thermogravimetric analysis [43].

2.3 Corrosion of Interconnects

As mentioned in Chapter 2.1.2, interconnects are a vital part of any fuel cell, where they electrically connect separate cells. Nowadays, the state-of-the-art interconnect material for solid oxide fuel cells is ferritic stainless steel. However, due to the harsh conditions during the operation of a SOFC, the interconnects degrade over time. Therefore, in the following, corrosion issues regarding interconnects as well as means to avoid these issues, such as adding alloying elements or applying coatings, are discussed.

2.3.1 Ferritic Stainless Steels as Interconnects

High temperature materials commonly rely on the formation of either a protective Al_2O_3 or a protective Cr_2O_3 scale. While alloys that form Al_2O_3 are extremely resistant against high temperature corrosion, alloys that form Cr_2O_3 suffer some disadvantages, such as continuous Cr evaporation [15]. However, the main function of an interconnect is to electrically connect separate cells, therefore, the interconnect must be an electron conductor, and, because Al_2O_3 is an insulator, Al_2O_3 forming alloys cannot be used as interconnect materials. Hence, the materials of choice for an interconnect are Cr_2O_3-forming steels, namely stainless steels.

There are many different types of stainless steels, and they are classified according to their crystalline structure. Two commonly used types are austenitic stainless steels, with a face-centered cubic (FCC) structure and ferritic stainless steels, with a body-centered cubic (BCC) structure [59]. The main materials used for interconnects today are the latter, because the thermal expansion coefficients (TEC) of ferritic stainless steels are much closer to other fuel cell components, especially the anode, than the TEC of austenitic stainless steels [40, 60]. Ferritic stainless steels typically have a Cr-content above 10 % and below 26 % [41], and a Cr-content above 16 % is desirable for use as an interconnect.

Specific alloys have been developed to be used as ferritic stainless steel interconnects, for example, Crofer 22 APU, Crofer 22 H, and Sanergy HT. These alloys typically have a Cr content of at least 21 % and other alloying elements, such as Mn and reactive elements, which are added to avoid specific interconnect-related issues and will be discussed below [61]. However, the major drawback of materials specifically designed for interconnects is their high cost. Therefore, other cheaper and commercially available steels are becoming more important in interconnect research. For example, AISI 441 or AISI 430 with Cr contents between 16 % and 20 % are gaining more attention [20, 21, 59, 62–70]. The general consensus is that these commercial steels are probably more suited for lower SOFC operating temperatures [59] around 600 °C to 700 °C because, at higher temperatures, the Cr content might not be sufficient for a long life-time.

Some of the most common alloying elements in interconnect materials and their positive effects are discussed in the following. These alloying elements are nearly always found in materials specifically designed for interconnects, and, most of the time, they are also present in commercially available steel grades, e.g. AISI 441, or AISI 430, which are being proposed as interconnect materials by different research groups.

Mn against Cr evaporation As mentioned in Chapter 2.2.4, stainless steels that form a protective Cr_2O_3 scale suffer from Cr-evaporation in air, especially under humid conditions. This process also occurs on the air-facing side of an interconnect in SOFCs, as humidity levels around 3 % are common. The evaporation of hexavalent Cr species leads to two issues for the fuel cell lifetime: Cr-deficiency in the interconnect followed by subsequent interconnect failure and Cr-poisoning of the cathode [36]. One simple way to decrease the Cr-evaporation in an interconnect is achieved by adding Mn to the alloy. This addition results in the formation of a $(Cr,Mn)_3O_4$ top layer with a continuously growing Cr_2O_3 layer beneath it [61, 71, 72]. Even small amounts of up to 0.5 weight% Mn in the alloy lead to a decrease in Cr-evaporation by a factor of 2 to 3 [61, 71].

Si and Nb, Mo or W Small amounts of Si are present in many ferritic stainless steels. While these amounts are not an issue for many applications, in interconnects the formation of a continuous SiO_2 layer could lead to a drastic increase in electrical resistance of the oxide scale. Therefore, materials that are specifically designed for interconnect use, employ methods to avoid SiO_2 formation. Either Si in the alloy is avoided to a great extent by a vacuum induction melting process, or other alloying elements are added to bind the Si. While Crofer 22 APU employs the former method, Crofer 22 H and Sanergy HT use the latter one. To bind the Si, alloying elements, such as Nb, Mo, or W, are added, which results in the formation of Laves phase precipitates. These Laves phases have the positive side effect that they increase the hardness and the creep strength of the steel [73, 74].

Reactive Elements Reactive elements (RE), such as Ce, La, Hf, and Y, are often added to high temperature materials. These elements are known to greatly improve oxide-scale adhesion and decrease oxide-scale growth [15, 16]. The mechanism for how these reactive elements work is not yet fully understood. But the general consensus is that the addition of REs leads to a decrease in cation diffusion through the oxide scale, and, therefore the oxide scale becomes more inward growing. Further information on the reactive element effect can be found in [75–78].

2.3.2 Coatings as a Means to Mitigate Corrosion

Two main degradation mechanisms, which stem from the corrosion of the interconnect, are responsible for fuel cell failure after a long lifetime. First, the Cr-evaporation of the interconnect leads to Cr-poisoning of the cathode (see Chapter 2.2.4), and, second, the continuous growth of the Cr_2O_3 scale leads to an increase in the electrical resistance of the interconnect [42]. Adding alloying elements, such as Mn, to decrease Cr-evaporation is only effective to a certain extent, and additional protection is needed. The addition

of other alloying elements requires specifically designed steels, which, as mentioned in Chapter 2.3.1, increases the cost of the interconnect. Therefore, nowadays, coatings are the norm for any interconnect material.

Different coating materials exist, and perovskite or spinel oxides are often suggested. Even though perovskites possess high electrical conductivities and good compatibility with other SOFC components, thick perovskite coatings are required to decrease the oxidation rate, and the coating is often poorly adhesive. Additionally, the positive effect of perovskite coatings on Cr-evaporation is limited [11, 72, 79, 80]. Therefore, the more commonly used coatings are spinel oxides, which have been shown to be highly efficient in mitigating Cr-evaporation. The most prominent spinel coating that has been suggested is $(Mn,Co)_3O_4$ (MCO), which shows promising Cr-retention [12–14], and, at the same time, it has rather high electrical conductivities (see Table 2.2) [81]. This coating cannot only be applied using powder-based methods, such as screen printing [82], spray coating [83], or electrophoretic deposition [84], but also via a conversion coating route [72, 85]. Conversion coatings are metal coatings that oxidize during high temperature exposure and, thus, form a ceramic coating. To achieve an MCO coating via conversion coating, the steel is first coated with Co, which then oxidizes to form Co_3O_4. Through the subsequent outward diffusion of Mn from the steel substrate, enrichment of the oxide layer with Mn takes place, and MCO is formed [66, 72, 85, 86]. This process has been well documented above 800 °C, however, limitations are possible at lower temperatures, as Mn diffusivity decreases. *Falk-Windisch* et al. [87] have shown that, at 650 °C, only 2-3 % Mn were present in the outer Co_3O_4 layer, and, instead, a Mn- and Cr-rich oxide had formed at the metal-oxide interface. Nevertheless, they could also prove that this had no negative effect on either the Cr-evaporation rate or the area specific resistance, and, in reality, both are lower at 650 °C than at 750 °C and 850 °C [87]. The advantages of Co conversion coatings are that very thin and dense coatings can be achieved, and, additionally, the process is highly cost effective as large-scale roll-to-roll coating applications are possible before the interconnect is deformed into its shape [88].

As mentioned in Chapter 2.3.1, a reactive element effect can be found for elements such as Ce, La, and Y. It has been shown that REs are not only effective as alloying elements but also as a coating material [16, 89]. Ce/Co coatings combine the positive effects of both, the MCO coating and a reactive element coating, and coatings with a 10 nm-thick Ce layer beneath a 640 nm-thick Co layer are very popular and can be considered as state-of-the-art coating [19].

2.3.3 Electrical Conductivity of Oxide Scales

The main function of an interconnect is to electrically connect fuel cells to each other. Therefore, its main property is to conduct electrons. However, even though metallic interconnects are highly conductive, the formation of a poorly conductive oxide scale during high temperature exposure immensely increases the overall resistance.

To describe the electrical conductivity of any oxide scale, the sum of the electronic and ionic charge carriers is calculated according to Equation 2.16,

$$\sigma_{total} = \sigma_{ionic} + \sigma_{electronic} = \sigma_{total}\left(t_{ionic} + t_{electronic}\right), \tag{2.16}$$

where σ_{total} is the total electrical conductivity, and σ_{ionic} and $\sigma_{electronic}$ are the respective conductivities, which are defined by Equations 2.17 and 2.18 with the transport numbers t_{ionic} or $t_{electronic}$ [43].

$$\sigma_{ionic} = \sigma_{total} \cdot t_{ionic}, \tag{2.17}$$

$$\sigma_{electronic} = \sigma_{total} \cdot t_{electronic}, \tag{2.18}$$

The electronic conductivity $\sigma_{electronic}$ is defined according to Equation 2.19 as the sum of the conductivity of the electrons σ_e and holes σ_h.

$$\sigma_{electronic} = \sigma_e + \sigma_h = e(nv_e + pv_h), \tag{2.19}$$

where n and p are the concentrations of electrons and holes, respectively, and v_e and v_h are the corresponding electron and hole mobilities [43]. Similarly, the total ionic conductivity σ_{ionic} is defined as the sum of the anion and cation conductivities [43].

Both the mobility and the concentration terms define the temperature dependency of the overall conductivity. At high temperatures, the electronic conductivity is mainly dependent on the concentration term, and, for oxides, this term increases with temperature. Therefore, in contrast to metallic conductors, the conductivity for metal oxides increases with higher temperatures. Oxides for which this is true, for example Cr_2O_3 and Co_3O_4, are classified as semiconductors [43]. The Arrhenius equation (Equation 2.20) can be used to describe the temperature dependency of an oxide scale.

$$\sigma = \sigma_0 \cdot \exp\left(\frac{-E_a}{R \cdot T}\right), \tag{2.20}$$

where σ_0 is a pre-exponential factor, R is the ideal gas constant, T is the absolute temperature, and E_a is the activation energy.

Typically, oxide scales on interconnects are discussed in terms of resistance instead of conductivity. The resistance R is defined by the following equation (Equation 2.21).

$$R = \frac{1}{\sigma} \cdot \frac{L}{A}, \tag{2.21}$$

where σ is the conductivity, L is the oxide thickness, and A is the measured area. The area specific resistance (ASR) especially is a common value used to describe the conductivity of an interconnect, as it is independent of the area (see Equation 2.22).

$$ASR = A \cdot R_{tot}. \tag{2.22}$$

Conductivity of Cr_2O_3 Cr_2O_3 is an intrinsic semiconductor at high temperatures above approximately 1 000 °C, below that, however, it exhibits extrinsic semi-conducting behavior, and, therefore, is reliant on dopants [90, 91]. Reported conductivity values for Cr_2O_3 reflect this change in behavior. While conductivities reported above approximately 1 000 °C show very similar values, the conductivities reported below that temperature

differ quite dramatically from publication to publication, and conductivities between 0.001 and 0.05 S cm^{-1} have been reported at 800 °C [91–99]. This large spread is reflected in the published activation energies for Cr_2O_3 with values ranging from 0.25 to 0.82 eV for measurements below 850 °C [91, 94–99].

It is not yet clear which doping mechanism prevails in Cr_2O_3, but it has been well documented that it is a dual semi-conductor with n-type or p-type semiconducting behavior [100], depending on if the structure is oxygen- or metal-deficient. The change in oxygen activity in thermally grown Cr_2O_3 throughout the scale has been found to result in dual oxide morphology [90, 91]. This duality is also often expressed in semi-conducting behavior. For example, *Latu-Romain* et al. [100–103] have found that, above 800 °C, the internal subscale is always an n-type semiconductor, while the outer subscale can be either an n-type or a p-type semiconductor, depending on the oxygen partial pressure. Another factor that strongly influences the conductivity of thermally grown Cr_2O_3 is doping from other alloying materials such as Fe, Mn, or Ti. This doping usually increases the conductivity of Cr_2O_3 [104, 105].

Conductivity of Spinels Another large class of oxides that is relevant for interconnects are spinels, which are used as interconnect coatings. Therefore, it is important to understand how electron conduction in spinels works and which spinels are highly conductive and, therefore, suited as interconnect coatings. It is generally assumed that spinels conduct electrons via a hopping mechanism between octahedral sites [106]. Therefore, good spinel conductors typically have elements that can accomodate different valence states on the octahedral sites. This also explains why Cr-containing spinels often exhibit low electrical conductivities because, in the spinel structure, the only possible oxidation state for Cr is Cr^{3+}, which has a very strong preference for occupying octahedral sites [107]. An extensive overview of the conductivities of different spinels was published by *Petric* et al. [81] (see Table 2.2). They showed that especially Mn- and Co- or Mn- and Cu-containing spinels show rather high conductivity and are, therefore, best suited for interconnect applications. On the other hand, $Mn_{1.2}Cr_{1.8}O_4$ has a very low electrical conductivity, which is in agreement with the aforementioned limitation of Cr-containing spinels. Similarly, low conductivity values have been reported for $MnCr_2O_4$ ($\sigma_{800\,°C} = 0.004\,S\,cm^{-1}$ [108] or $\sigma_{800\,°C} = 0.03\,S\,cm^{-1}$ [109]) and $Mn_{1.7}Cr_{1.3}O_4$ ($\sigma_{800\,°C} = 0.14\,S\,cm^{-1}$ [108]). These low conductivities can be an issue for interconnects that rely on the formation of a $(Cr,Mn)_3O_4$ as a protective barrier against Cr-evaporation. Therefore, coatings that avoid the formation of these poorly conductive spinels are preferred as interconnect coatings.

2.3.4 Dual Atmosphere Effect

Component testing, for example the testing of interconnect materials, is commonly done in a single atmosphere, i.e. either fuel-side atmosphere or air-side atmosphere. However, the interconnect in a fuel cell is exposed to a dual atmosphere as shown in Figure 2.5.

There have been many different publications [17, 110–113] in the early 2000s that have analyzed how dual atmosphere affects corrosion behavior. Most researchers have reported increased corrosion on the air-facing side of ferritic stainless steels at 800 °C, when hydrogen is present on the other side of the steel. This is compared to when the

Table 2.2: Conductivity values for different transition metal spinels measured at 800 °C unless stated otherwise. Data taken from [81]. The conductivities are given in $S\,cm^{-1}$. The most relevant spinel conductivities for this work are marked in bold.

	Mg	Mn	Co	Ni	Cu	Zn
Al	$MgAl_2O_4$ $\sigma = 10^{-6}$	$MnAl_2O_4$ $\sigma = 10^{-3}$	$CoAl_2O_4$ $\sigma = 10^{-5}$	$NiAl_2O_4$ $\sigma = 10^{-4}$	$CuAl_2O_4$ $\sigma = 0.05$	$ZnAl_2O_4$ $\sigma = 10^{-6}$
Cr	$MgCr_2O_4$ $\sigma = 0.02$	**$Mn_{1.2}Cr_{1.8}O_4$** $\sigma = 0.02$	$CoCr_2O_4$ $\sigma = 7.4$	$NiCr_2O_4$ $\sigma = 0.73$	$CuCr_2O_4$ $\sigma = 0.40$	$ZnCr_2O_4$ $\sigma = 0.01$
Mn	$MgMn_2O_4$ $\sigma = 0.97$	Mn_3O_4 $\sigma = 0.10$	**$CoMn_2O_4$** $\sigma = 6.4$	$NiMn_2O_4$ $\sigma = 1.4$	$Cu_{1.3}Mn_{1.7}O_4$ $\sigma = 225$ (750 °C)	$ZnMn_2O_4$
Fe	$MgFe_2O_4$ $\sigma = 0.08$	$MnFe_2O_4$ $\sigma = 8.0$	$CoFe_2O_4$ $\sigma = 0.93$	$NiFe_2O_4$ $\sigma = 0.26$	$CuFe_2O_4$ $\sigma = 9.1$	$ZnFe_2O_4$ $\sigma = 0.07$
Co		**$MnCo_2O_4$** $\sigma = 60$	**Co_3O_4** $\sigma = 6.7$			

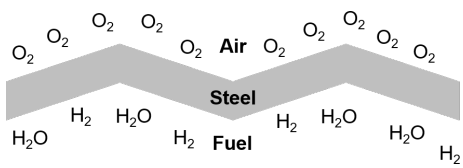

Figure 2.5: *Dual atmosphere to which the interconnects in a solid oxide fuel cell are subjected.*

steel is only exposed to air atmosphere. For example, *Yang* et al. [17] have reported that, under isothermal conditions, the Cr rich Crofer 22 APU (23 % Cr) formed an iron-rich spinel top layer, while AISI 430, which has only 17 % Cr, even showed the formation of Fe_2O_3 nodules on the air-facing side. Even though other studies have also reported iron enrichment in the oxide scale in dual atmosphere [110] or the formation of thicker oxide scales [111, 113], the formation of hematite nodules has only been reported in some cases [17, 112]. Some studies have not found any significant effect of dual atmosphere on corrosion behavior [21, 114]. Except for the study by *Alnegren* et al. [21], all these studies have focused on high temperatures around or above 800 °C, although the trend nowadays is towards lower operating temperatures for SOFCs.

The trend towards lower temperatures is mainly explained by the expectation that these lower temperatures will reduce material degradation, and, thus, allow for the use of cheaper materials. However, some studies conducted at lower temperatures in either anode or cathode simulating atmospheres have not confirmed this. For example, *Young* et al. [115] have found more corrosion of ferritic stainless steel at 500 to 600 °C than at 650 to 800 °C in simulated anode atmosphere. *Niewolak* et al. [59] have also reported the

formation of breakaway oxidation on ferritic and austenitic stainless steels at 600 °C in anode-simulated atmosphere. In steam atmosphere ($Ar + 50\,\%H_2O$), *Zurek* et al. [116] have found that different FSSs with Cr contents between 9-12 %Cr showed different oxidation behaviors between 550 and 650 °C. While some steels oxidized faster at 650 °C than at 550 °C, other steels showed exactly the opposite behavior and even formed less-protective, iron-rich oxides at 550 °C. Those authors assert that, at lower temperatures, either the "enhanced in-scale diffusion and surface reaction kinetics" result "in an increase of the oxidation rate", or the "enhanced incorporating of Cr in the scale" result "in a decrease of the oxidation rate" [116]. *Sanchez* et al. [117] have reported that AISI 430 forms a Cr_2O_3 scale at 800 °C, but a $(Fe,Cr)_2O_3$ scale at 650 °C. Their reasoning is the reduction in Cr diffusion at lower temperatures, which is in agreement with the conclusion of *Zurek* et al. [116].

These results at lower temperatures have warranted *Alnegren* et al. to re-examine the dual atmosphere effect. For the commercially available steel AISI 441, they found a severe dual atmosphere effect at 600 °C [20] with the formation of breakaway oxidation on most parts of the exposed samples, while samples exposed to single atmosphere showed no signs of breakaway oxidation. Additionally, they also showed that this effect is temperature inverse, i.e. a more pronounced effect was observed at lower temperatures (600 °C) than at higher temperatures [21]. *Alnegren* et al. have suggested that the inverse temperature dependency is due to a reduction in Cr diffusivity in the bulk at lower temperatures, which could result in Cr deficiencies beneath the oxide scale and, thus, the formation of breakaway oxidation.

Even though the mechanism for the dual atmosphere effect is still not understood in detail, what is certain is that hydrogen is the cause of this effect. This is corroborated by the high diffusivity of hydrogen through ferritic stainless steels, which is extremely fast, and, at 800 °C, rates in the $mm\,h^{-1}$ range can be expected [114, 118, 119]. Furthermore, *Bredvei Skilbred* et al. [110] have reported that, for Sanergy HT at 800 °C, an increase in hydrogen levels was found in the oxide layer on the air-facing side for samples that were exposed to dual atmosphere, compared to samples that were exposed to "air-only" atmosphere. This further suggests that the hydrogen does diffuse through the alloy.

Different theories have been proposed as to where the hydrogen attacks. *Yang* et al. [17, 120], for example, have suggested that, due to the formation of hydroxides in the oxide scale, accelerated Fe diffusivity occurs, which leads to the formation of iron-rich oxide scales or even Fe_2O_3. They have reported that - with the assumption of Cr_2O_3 being a p-type semiconductor under oxidizing conditions [91] - metal vacancies could form to compensate for the positive charge created by the substitution of an oxygen anion with a hydroxide. Due to the metal vacancies, the cation diffusivity could be greatly enhanced in the scale. *Yang* et al. [17, 120] have also reported that this is in agreement with earlier studies by *Tveeten* et al. [121], who have shown that the presence of hydrogen in Cr_2O_3 greatly enhances the Cr cation diffusivity in the oxide.

Rufner et al. [111] have proposed that, in addition to enhanced cation diffusivity in the oxide scale as suggested by *Yang* et al. [17], the oxygen activity could also be altered by the presence of hydrogen. *Bredvei Skilbred* et al. [110] have mentioned that Fe diffusivity could be increased by the presence of hydrogen, but they have additionally suggested that hydrogen could form steam inside the oxide scales, which at high pressures

could lead to pore formation and, thus, faster scale growth and an increase in oxygen inward diffusion. The latter theory has also been proposed by *Holcomb* et al. [122].

Chapter 3

Materials and Methods

3.1 Materials

The composition of all materials used in this work, including their respective thicknesses, can be found in Table 3.1 and Table 3.2.

Table 3.1: Material composition of ferritic stainless steel Crofer 22 APU (EN 1.4760) in weight%.

	Fe	Cr	Mn	Si	Ti	C	S	Al	Cu	P	La
Crofer 22 APU Batch: 173288 Paper I Thickness: 0.3 mm	Bal.	22.92	0.38	0.01	0.06	0.004	<0.002	0.01	0.01	0.005	0.09

Table 3.2: Material composition of all studied AISI 441 (EN 1.4509) batches in weight%.

	Fe	Cr	Mn	Si	Ti	Nb	Ni	C	S	N
AISI 441 Batch 64313 (hereafter A) Paper II/III Thickness: 0.2 mm	Bal.	17.74	0.30	0.55	0.15	0.37	0.19	0.015	0.002	-
AISI 441 Batch 63960 (hereafter B) Paper II Thickness: 0.2 mm	Bal.	17.83	0.26	0.55	0.14	0.48	0.13	0.012	0.002	0.016
AISI 441 Batch 64534 (hereafter C) Paper III Thickness: 0.3 mm	Bal.	17.56	0.35	0.59	0.17	0.39	0.26	0.014	0.001	0.017

Specific sample geometries were required and different coatings were examined, depending on the experiment conducted. This data is shown in Table 3.3. All coatings were

applied with physical vapor deposition (PVD) by AB Sandvik Materials Technology. In Paper I, a short pre-oxidation (3 min in air at 900 °C) was conducted prior to coating. This was done to suppress the outward diffusion of iron into the Co-oxide layer as reported previoulsy by *Falk-Windisch* et al. [87, 123]. For Paper III, some of the samples were first pre-oxidized and, subsequently, the pre-oxidation layer was removed by grinding (grit P1200) the hydrogen-facing side, the air-facing side, both sides, or no side. Except for the case in which no pre-oxidation layer was removed, the resulting thickness of each sample was approximately 0.2 mm. Before exposure, all materials were cleaned ultrasonically in acetone and ethanol.

Table 3.3: Sample geometries and applied coatings for all conducted experiments. [*1] Samples were exposed by AB Sandvik Materials Technology; [*2] Ground on air-facing side, hydrogen-facing side, no side, or both sides.

Material Paper	Coating Inner	 Outer	Geometry	Surface modification	Exposure conditions
Crofer 22 APU Paper I	Pre-oxidation 3 min 800 °C air	After Pre-ox 600 nm Co 1 500 nm Co 3 000 nm Co	15 x 15 mm	as-received	500 h 600 °C stagnant laboratory air
AISI 441 Batch A & B Paper II	10 nm Ce	640 nm Co	30 x 40 mm	as-received	up to 37 000 h [*1] 800 °C box [*1] or tube furnace
AISI 441 Batch B Paper II	uncoated		30 x 20 mm	as-received	up to 3 000 h 800 °C tube furnace
AISI 441 Batch A Paper III	uncoated Pre-oxidation in air at 800 °C for 0, 11, 45, 180, or 280 min		Circular $\varnothing$ = 21 mm	as-received	500 - 1 000 h 600 °C dual atmosphere
AISI 441 Batch C Paper III	uncoated Pre-oxidation in air at 800 °C for 180 min		Circular $\varnothing$ = 21 mm	ground [*2] grit P1200	500 h 600 °C dual atmosphere

3.2 Exposures

The exposure conditions, including temperatures and atmospheres, for all exposures conducted in this work can be found in Table 3.3. Unless otherwise stated, all exposures were carried out in tube furnaces (see Figure 3.1a). The experimental setup of a tube furnace is shown in Figure 3.2.

For Paper I all samples were exposed in a tube furnace, and stagnant laboratory air was used (see Table 3.3). The exposed samples were characterized after exposure using x-ray diffraction (XRD), scanning electron microscopy/energy dispersive x-ray spectroscopy (SEM/EDX), broad-ion beam milling (BIB), and area specific resistance (ASR) measurements.

More complex setups were used for all other exposures, which are explained in more detail in the following.

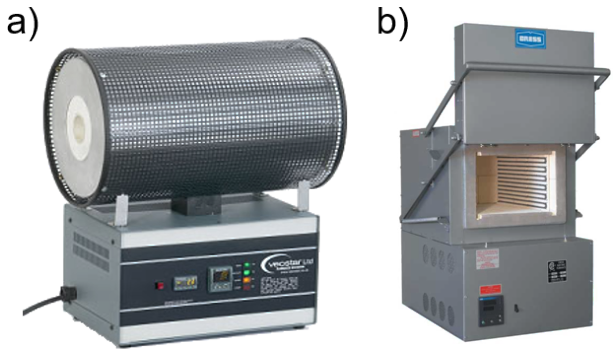

Figure 3.1: *Different furnaces used for exposures. a) Tube furnace used for short-term exposures and Cr-evaporation measurements, b) Box furnace used for long-term exposures performed by AB Sandvik Materials Technology.*

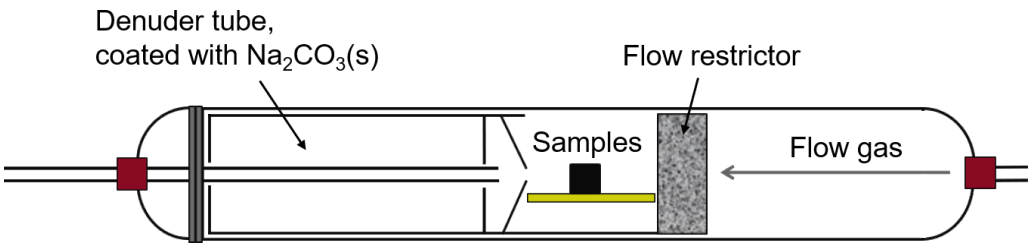

Figure 3.2: *Experimental setup for tube furnace exposures and Cr-evaporation measurements based on Froitzheim et al. [124].*

3.2.1 Long-Term Exposures

All long-term exposures ($t_{exposure} > 3\,000$ h) were performed by AB Sandvik Materials Technology (SMT). The samples were exposed at 800 °C in a box furnace. The two different furnaces available for exposures can be seen in Figure 3.1: tube furnace (Figure 3.1a) and box furnace (Figure 3.1b). Both furnaces have different advantages and are, thus, used for different experiments. The main advantage of a box furnace is that it allows for a high throughput of samples, thus decreasing the experiment cost. Therefore, this furnace is favored for long-term exposures. The drawbacks of this furnace type are that the atmosphere and the direct temperature the samples are exposed to is not fully controllable. On the other hand, tube furnaces have limited capacities with a maximum of three samples for Cr-evaporation measurements and six samples for other exposures. However, tube furnaces allow for well-defined exposure conditions with exact temperatures and a controlled atmosphere with a predefined flow and humidity.

Because of these advantages and disadvantages long-term exposures ($t_{exposure} > 3\,000$ h) of Ce/Co-coated AISI 441 were carried out in box furnaces. The mass gain was recorded regularly by AB Sandvik Materials Technology. This resulted in discontinuously exposed samples. For further analysis, such as microstructural analysis, Cr-evaporation measurements, and ASR measurements, samples were taken out after 7 000 h, 23 000 h, 35 000 h, and 37 000 h. Two different AISI 441 batches were used for these long-term exposures (see Table 3.2). Batch A was exposed for 37 000 h and was, subsequently, used for Cr-evaporation measurements, whereas batch B was exposed for 7 000 h, 23 000 h, and 35 000 h, and, subsequently, area specific resistance values were recorded. To have Cr-evaporation data and ASR values for samples exposed for shorter times, Ce/Co-coated AISI 441 (batch B) and uncoated AISI 441 (batch A) were additionally exposed isothermally in a tube furnace for 1 000 h. Ce/Co-coated AISI 441 (batch B) was also exposed isothermally for 3 000 h in a tube furnace, and ASR values were subsequently obtained. All tube furnace exposures were conducted in air/3 % H_2O and a flow rate of 6 000 sml $\cdot$ min^{-1}.

3.2.2 Cr-Evaporation Measurements

As mentioned in Chapter 2.2.4, Cr-evaporation is a major issue for the longevity of a solid oxide fuel cell. Therefore, it is necessary to quantify the Cr-evaporation that occurs during the exposure of interconnects. *Froitzheim* et al. [124] have developed a method that allows for in-situ determination of Cr-evaporation. The basis for this method is Reaction 3.1 and the experimental setup in Figure 3.2.

$$CrO_2(OH)_2(g) + Na_2CO_3(s) \longrightarrow Na_2CrO_4(s) + H_2O(g) + CO_2(g) \tag{3.1}$$

The coated denuders (see Figure 3.2) were exchanged regularly during exposure. They were then rinsed with deionized water and the Cr concentration in the solution was quantified with UV-VIS spectrophotometry (see Chapter 3.3.1). A high air flow of 6 000 sml $\cdot$ min^{-1} ensured kinetically controlled and, thus, flow-independent Cr-evaporation [124]. As can be seen in Equations 2.14 and 2.15, the formation of volatile Cr-species, such as $CrO_2(OH)_2$, is dependent on the presence of H_2O, therefore, 3 % water vapor was employed for all Cr-evaporation measurements. Three 1.5 x 1.5 cm samples were measured at the same time. However, long-term exposed samples that were provided by Sandvik Materials Technology were 3 x 4 cm and, therefore, too large. These samples were cut-down to 3 x 2 cm with a low-speed saw to achieve a similar surface area and so that the samples would fit in the furnace.

3.2.3 Dual Atmosphere Exposures

Dual atmosphere exposures were conducted to investigate the dual atmosphere effect with a particular focus on pre-oxidation. The sample holder visualized in Figure 3.3 was used to expose samples to a dual atmosphere. This sample holder was based on a design from Montana State University. Further detailed information about the dimensions of the sample holder can be found in [111, 112, 122]. The sample holder had a total of six sample slots, three on one side (visible in Figure 3.3) and three on the other side (not visible in Figure 3.3). Gold gaskets were used to ensure gas tightness, and tightness was

controlled before and during exposure. The six samples could be exposed simultaneously either to dual atmosphere or three samples to dual atmosphere and three samples to single atmosphere. Gas compositions and flow rates are given in Figure 3.3. The humidity of each gas was achieved by bubbling the gas through water heated to 24.4 °C, which leads to a humidity of 3 % water vapor. All dual atmosphere exposures were conducted at 600 °C.

Two different experiments were conducted to determine the role of pre-oxidation in dual atmosphere exposures. All pre-oxidations were achieved at 800 °C in a low and humid air flow (3 % H_2O). Further details for both experiments are given in the following.

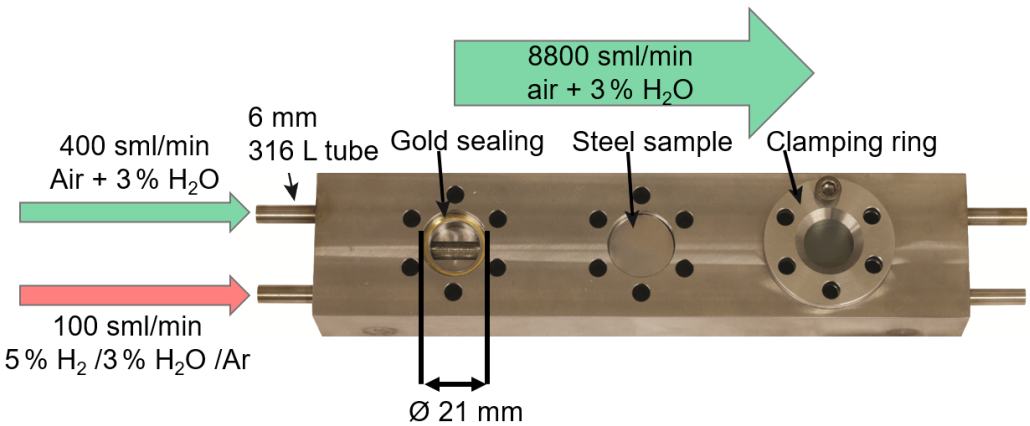

Figure 3.3: *Dual atmosphere sample holder.*

Pre-oxidation Time Five different pre-oxidation times were used to determine the influence of pre-oxidation time on corrosion behavior: 0 min, 11 min, 45 min, 180 min, and 280 min. The exposure was run discontinuously for 1 000 h. The exposure was interrupted after 24 h, 168 h, 500 h, and 730 h to document the progress of corrosion, and photos were taken of all samples. After exposure, more extensive analysis with SEM/EDX was conducted of the top view and cross sections prepared with BIB.

Pre-oxidation Location To understand if the pre-oxidation layer on the hydrogen-facing side or the pre-oxidation layer on the air-facing side is more beneficial for the mitigation of the dual atmosphere effect, samples were first pre-oxidized for 180 min. Subsequently, the pre-oxidation layer was removed from both sides, the air-facing side or the hydrogen-facing side, by grinding with grit P1200. The pre-oxidation layers on both sides of one sample were left intact. Double samples were prepared for the most relevant cases, i.e. the pre-oxidation layer present on the air-facing side or the hydrogen-facing side. The summarized scheme for this experiment is shown in Figure 3.4. The dual atmosphere exposure was run isothermally for 500 h. After exposure, extensive analysis with SEM/EDX was conducted on the sample surface and on cross sections prepared with BIB.

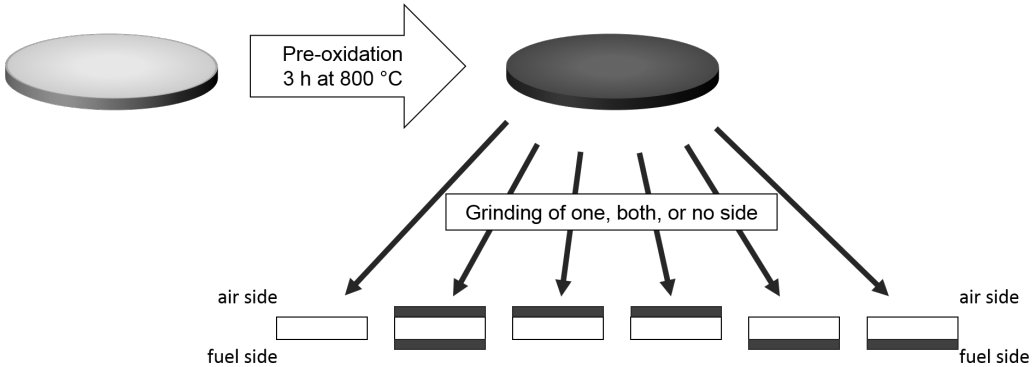

Figure 3.4: *Scheme for pre-oxidation location experiment [125]. AISI 441 samples were first pre-oxidized for 3 h at 800 °C in air, and then the oxide layer was removed by grinding (grit P1200).*

3.3 Analytical Methods

After exposure, different analytical methods were employed to examine and characterize the progress of corrosion. Different techniques are described further in the following, and specifics about the instruments used are given.

3.3.1 Spectrophotometry

Quantification of light-absorbing ions or molecules in a solution can be achieved with spectrophotometry. This technique is based on the fact that the intensity of light passing through a solution containing light-absorbing molecules or ions will be reduced. To measure this absorbance, a photometer is used. The Beer-Lambert law (see Equation 3.2) describes the relation between the absorbance A and the concentration of the light-absorbing species c.

$$A = \log_{10} \frac{I_0}{I} = \varepsilon_\lambda \cdot c \cdot l, \tag{3.2}$$

where I_0 is the initial light intensity, I is the light intensity after passing through the cuvette, ε_λ is the wavelength-dependent molar absorption coefficient, and l is the path length through the sample (cuvette thickness).

Hexavalent Cr solutions obtained with the Cr-evaporation measurements were analyzed using this technique, and the concentration of Cr could be determined. These Cr(VI)-solutions exhibited a high absorption at $\lambda = 370\,nm$, therefore, all measurements were carried out at that wave-length. Further details on this analysis technique can be found in [126].

3.3.2 Area Specific Resistance

Area specific resistance (ASR) measurements were conducted in Papers I and II to examine the dependence of resistance on the thickness of the oxide layers present in exposed samples. Only ex-situ measurements were conducted. This was done due to previously published results by *Grolig* et al. [67, 92], who had observed an effect of Pt on the overall resistance of a sample during in-situ measurements.

To measure the ASR value of an exposed sample, an area of $1 \times 1\,cm^2$ was sputter coated with a roughly 100 nm thin Pt layer using the Quorom 150 sputter coater and, subsequently, the sputtered area was painted with platinum paste (Metalor 6926). Afterwards, the samples were dried at 150 °C for 10 min and then sintered at the exposure temperature for 1 h to remove all remaining binders from the Pt paste. This process is illustrated in Figure 3.5. To measure the ASR values, a NorECs Probostat (Norway) in combination with a Keithley 2400 source meter was used for four-point probe measurements in DC mode (see Figure 3.6). A current of 100 mA was chosen for all measurements, and the ASR was measured at the exposure temperature and during the cooling period to verify semi-conducting behavior. More details on the measurement setup can be found in [67, 92].

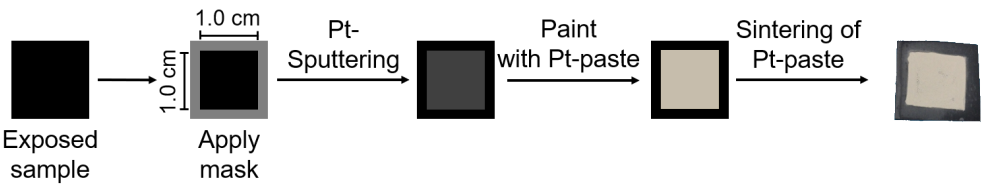

Figure 3.5: *Schematic drawing of the electrode preparation process [92].*

3.3.3 X-Ray Diffraction

X-ray diffraction is commonly used for structure analysis, phase identification, and analysis of phase composition of crystallized materials. With this technique, incoming monochromatic x-ray beams (for example CuK_α) are diffracted from the different lattice planes of a crystallized substance. A diffraction pattern is created by the scattered x-ray beams that were in phase, i.e. constructive interference, as only these show reasonable intensities. Constructive interference only occurs when the Bragg equation (see Equation 3.3) is fulfilled. This equation defines the relationship between the lattice plane spacing, d_{hkl}, and the angle in which the incoming x-ray beam meets the lattice plane, θ_{hkl} (see Figure 3.7a) [127].

$$n\lambda = 2d_{hkl} \sin \theta_{hkl}, \tag{3.3}$$

where n is an integer and λ is the x-ray beam wavelength.

All XRD patterns were recorded with Bragg-Brentano geometry (see Figure 3.7b) on a D5000 diffractometer with CuK_α radiation ($\lambda = 1.54178\mathring{A}$) and over the angular range

Figure 3.6: *ASR setup with a mounted sample pictured on the upper left side, the Probostat top is on the lower left side, and the entire setup, including furnaces is on the right side [92].*

$20^\circ \leq 2\theta \leq 70^\circ$. XRD was used for phase composition analysis of the oxide layers formed on exposed steel samples.

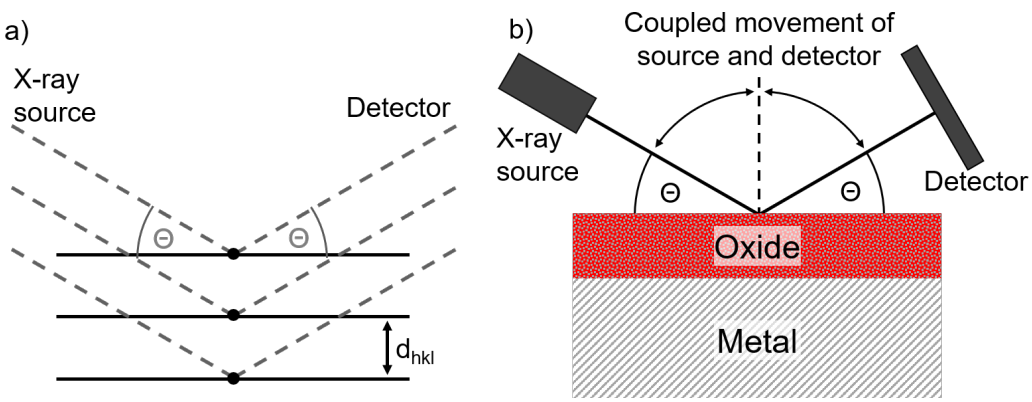

Figure 3.7: *Schematic drawing of a) Bragg's law and b) Bragg-Brentano geometry.*

3.3.4 Broad Ion Beam Milling

To prepare cross sections up to a millimeter scale without negatively impacting the thin oxide layers, a broad ion beam mill was used. Broad ion beam milling is achieved by bombarding ions, in this case Ar ions, onto a sample and, thus, slowly removing layer by layer of the sample surface. The resulting cross section is smooth and typically shows less mechanical damage than if other ways of preparing cross sections were used, such as mechanical polishing.

To properly protect the thin oxides and to achieve better contrast in subsequent SEM analysis, BIB samples were coated with a thin Au or Pt layer, and a Silicon wafer was glued on top. Prior to milling, the samples were cut in half perpendicular to the rolling direction of the material to ensure that the cross section is representative of the sample center. A Leica EM TIC 3 X and voltages around 6.5 keV were used. The resulting cross sections were then analyzed using SEM.

3.3.5 Scanning Electron Microscopy/Electron Dispersive X-Ray Spectroscopy

Scanning electron microscopy is a useful tool to analyze the microstructure of steel samples that have been exposed to high temperatures. In comparison to optical microscopy, the resolution of scanning electron microscopy is in the nanometer range, making it a useful tool to visualize the thin oxide layers that form on steel samples. In a scanning electron microscope, accelerated electrons interact with the surface layers of a sample. This interaction results in the excitation of different emissions, such as secondary electrons, backscattered electrons, or x-ray radiation, which can be separately detected by different detectors. To understand what information these different emissions give, it is important to know how they are generated (see Figure 3.8a-c) and what their interaction volume is, as each emission has a different interaction volume (see Figure 3.8d) [128–130]. Two different SEMs were used: a Zeiss Ultra 55 FEG-SEM and a FEI Quanta FEG 200 ESEM, both of which were equipped with an energy dispersive x-ray detector. Secondary and backscattered electrons were used for imaging purposes, and energy dispersive x-ray spectroscopy was used for compositional analysis. These signals are explained more closely in the following.

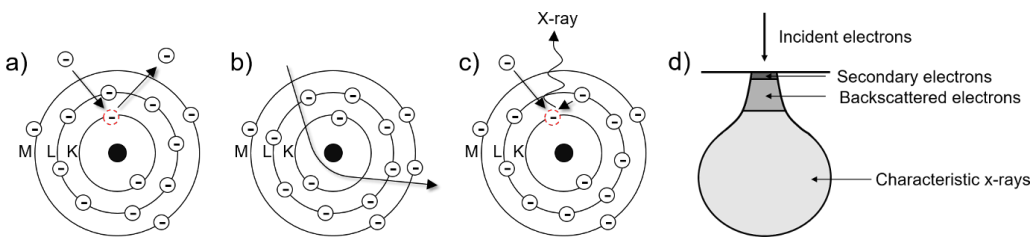

Figure 3.8: *Schematic drawing of how different SEM signals are produced (a-c) and their respective interaction volume (d). The three depicted SEM signals are a) secondary electrons, b) backscattered electrons and c) x-ray radiation [128, 129].*

Secondary Electrons Primarily secondary electrons are used to gain information about the surface topography, as these electrons only interact with the outermost surface of the sample (see Figure 3.8d) and are, subsequently, highly surface sensitive. They are generated by inelastic scattering of an incoming electron beam on an electron in an atom, thus ejecting the electron from the atom (see Figure 3.8a). The ejected electron is called the secondary electron and its energy is usually below 50 eV [130].

Backscattered Electrons Compositional information about the sample surface is given by backscattered electrons, as heavier elements lead to an increase in backscattered electrons and, subsequently, an increase in signal and in the brightness of the image. These electrons are generated by elastic scattering of the incoming electron beam on the atom nuclei (see Figure 3.8b). The energy of backscattered electrons is much higher than that of secondary electrons, leading to a higher interaction volume (see Figure 3.8d) and a lower image resolution [130].

Energy Dispersive X-Ray Spectroscopy EDX is used for more exact compositional information. To collect EDX spectrums, a primary electron beam ejects an electron from the inner shell of an atom. This void is then filled by an electron from an outer shell, and the energy difference between both shells is released as an x-ray photon with a specific energy (see Figure 3.8c). The energy of the x-ray photon is characteristic for each element as it is defined by the energy difference of the two shells, which depends on the atomic number and the energy levels that took part in the excited and relaxed states. Because x-ray radiation can penetrate the sample to a much further extent than secondary or backscattered electrons, the interaction volume of this radiation is much greater, and the resolution is much lower (see Figure 3.8d) [130].

Chapter 4

Results and Discussion

4.1 Influence of Cobalt Coating Thickness on the Area Specific Resistance

Different coatings are usually applied onto the substrate to increase corrosion resistance of ferritic stainless steels (see Chapter 2.3.2). However, how much different coatings influence the electrical conductivity of the interconnect is currently under discussion. As mentioned in Chapter 2.3.3, different oxides exhibit different conductivities, and sometimes adding a dopant increases the conductivity of an oxide scale immensely. Therefore, countless publications concentrate on increasing the conductivity of a coating [11, 18, 131–139]. However, in addition to the coating, the continuously growing Cr_2O_3 underneath the coating also contributes to the overall resistance of an interconnect. As mentioned in Chapter 2.3.3, the conductivity of Cr_2O_3 is extremely low compared to that of standard spinel coatings. For example, the moderately conductive Co_3O_4 has a conductivity of $\sigma_{Co_3O_4} = 6.7\,S\,cm^{-1}$ at 800 °C, which is still more than a factor of 100 greater than one of the highest recorded conductivities for Cr_2O_3 ($\sigma_{Cr_2O_3} = 0.05\,S\,cm^{-1}$ [90]). Therefore, the question arises does the conductivity of the coating even matter, or is its impact on the overall conductivity of the interconnect negligible compared to the impact of the thermally grown Cr_2O_3.

To investigate the influence of coating resistance on the overall resistance of an interconnect, three different Co coating thicknesses (600 nm, 1 500 nm, and 3 000 nm) on Crofer 22 APU were exposed in air at 600 °C for 500 h. These exposure settings were chosen as a worst-case scenario for interconnects in SOFCs, as the Cr_2O_3 layer is expected to be thin (below 100 nm) after this timeframe and at these low temperatures. The ASR was measured of all samples after exposure. If it is found that the oxidized Co coating contributes to the overall resistance of an interconnect, high ASR values should be measured for the thick Co coatings, and low ASR values should be measured for the thin Co coatings.

4.1.1 Microstructural and Compositional Analysis

The SEM micrographs (Figure 4.1a-d) for Co-coated Crofer 22 APU samples exposed for 500 h at 600 °C showed similar oxidizing behavior for all pre-oxidized samples. A thick Co_3O_4 toplayer was present, and, underneath this layer, a thin, roughly 35-45 nm thermally grown Cr_2O_3 had formed. While the Cr_2O_3 layer was roughly the same for all

pre-oxidized cases, the thickness of the outer Co_3O_4 layer was dependent on the Co-coating thickness. The three Co-coating thicknesses, 600 nm, 1 500 nm, and 3 000 nm resulted in 1.2 μm, 2.8 μm, and 5.7 μm thick Co_3O_4. The increase in volume of the coating is in line with the PBR value for Co (1.98, see Table 2.13). EDX analysis confirmed that the Co_3O_4 layer in all pre-oxidized cases was nearly pure, and only very low Cr ($< 0.9\,atomic\%$), Fe ($< 0.9\,atomic\%$), and Mn ($< 0.2\,atomic\%$) levels were detected. Spallation occurred on some of the samples with a 3 000 nm thick Co coating, therefore, a SEM micrograph of a non-spalled sample and one of a spalled sample are depicted in Figure 4.1c and d, respectively. Diffusion of Fe into the Co-coating of the non-pre-oxidized sample led to the formation of an additional $(Co,Cr,Fe)_3O_4$ layer between the Co_3O_4-layer and the thermally grown Cr_2O_3. This phenomenon has been discussed in great detail in [87] and [123].

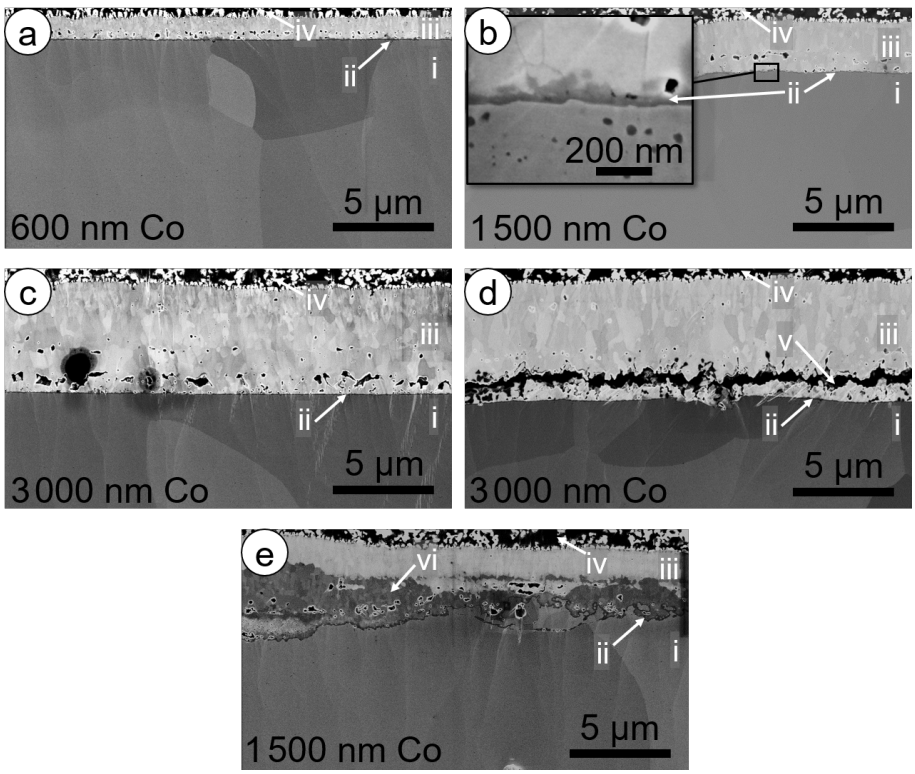

Figure 4.1: *SEM micrograph of cross sections of Co-coated Crofer 22 APU exposed for 500 h at 600 °C. All samples were Co-coated according to the following specifications: a) pre-oxidized sample with 600 nm Co coating, b) pre-oxidized sample with 1 500 nm Co coating, c) pre-oxidized sample with 3 000 nm Co coating, d) pre-oxidized sample with 3 000 nm Co coating, which showed signs of spallation after exposure, and e) non-pre-oxidized sample with 1 500 nm Co coating. The phases are identified as follows: i) substrate alloy, ii) Cr_2O_3, iii) Co_3O_4, iv) Pt electrode, v) spallation crack, and vi) $(Co,Cr,Fe)_3O_4$.*

Two phases were identified using XRD diffractometry for the pre-oxidized and non-pre-oxidized samples (Figure 4.2): the substrate, Crofer 22 APU (A), and the Co_3O_4 spinel phase (S). The reason why no other phases could be identified using XRD was probably due to the thickness of the Co_3O_4 layer. The thermally grown Cr_2O_3 was very thin in comparison to the Co_3O_4 layer (Figure 4.1). A more in-depth XRD analysis of non-pre-oxidized 1 500 nm Co-coated Sanergy HT, which was exposed at 650 °C, can be found in [123]. In this work the authors, *Falk-Windisch* et al. [123], carefully removed the upper Co_3O_4 layer by grinding, and all phases could be identified.

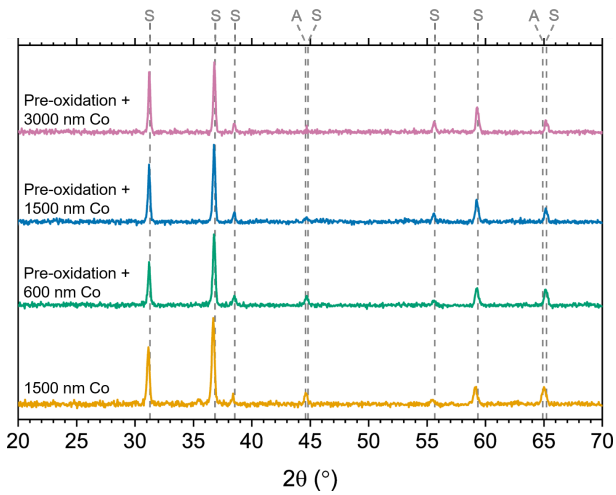

Figure 4.2: *X-ray diffractogram of Co-coated Crofer 22 APU exposed for 500 h at 600 °C. The phases were identified as follows: substrate alloy (A) and Co_3O_4 (S).*

4.1.2 Area Specific Resistance

The ASR values for all pre-oxidized, non-spalled samples were between 8 and 12 $m\Omega cm^2$, independent of the Co-coating thickness, and a rather small spread was observed (Figure 4.3). This strongly suggests that the Co coating did not significantly influence the overall conductivity of the interconnect.

The higher ASR values and their wide spread for pre-oxidized spalled samples (ASR between 16 to 37 $m\Omega cm^2$) and non-pre-oxidized samples (ASR between 23 to 50 $m\Omega cm^2$) can be explained by examining the SEM micrographs (Figure 4.1d and e). In the former samples, the spallation not only led to a loss of contact and subsequent higher ASR values, but, depending on the degree of spallation that occurred on each sample a wide spread was not surprising. On the other hand, in the latter samples the presence of a $(Co,Cr,Fe)_3O_4$ layer was probably the reason for both: high ASR values, due to the lower conductivity of the mixed spinel compared to the conductivity of the rather pure Co_3O_4, and the wide spread, due to the inhomogeneity of this mixed spinel layer and the big difference in thickness of this layer.

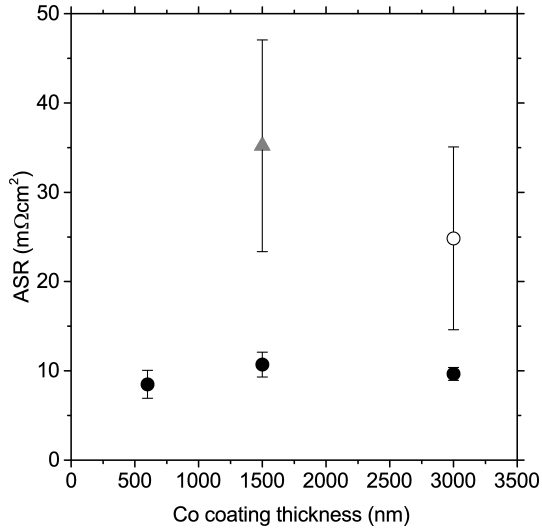

Figure 4.3: *Area specific resistance of Co-coated Crofer 22 APU exposed for 500 h at 600 °C. Circles correspond to samples that were pre-oxidized prior to Co coating and samples depicted as triangles were not pre-oxidized prior to Co coating. Empty symbols indicate samples that showed signs of spallation. Error bars indicate standard deviations.*

The experimental results - that in most cases the conductivity of the coating does not matter for the overall conductivity of the interconnect - was corroborated with calculations based on Equations 2.20, and 2.21, in Chapter 2.3.3 and literature values for the conductivities of Co_3O_4 and Cr_2O_3 (Table 4.1). The expected ASR values, according to the conductivity values in Table 4.1 can be calculated with Equation 4.1.

$$ASR_{cal} = 2 \cdot R_T(Co_3O_4) + 2 \cdot R_T(Cr_2O_3), \tag{4.1}$$

where the factor 2 is due to the fact that the oxide is formed on both sides, ASR_{cal} is the calculated ASR value, and $R_T(Co_3O_4)$ and $R_T(Cr_2O_3)$ are the resistance of the respective oxides at temperature T.

There are many reasons for the deviation of the experimental ASR ($ASR_{exp}(600\,°C) \approx 8\,m\Omega cm^2$) and the calculated ASR ($ASR_{cal}(600\,°C) = 3.38\,m\Omega cm^2$; according to Equation 4.1) for a 600 nm thick Co coating. These include impurities in the thermally grown Cr_2O_3, variations in the thickness of the Cr_2O_3 and/or Co_3O_4 layer and the presence of partial pressure gradients through the oxide layers. However, the greatest limitation for these theoretical calculations is probably the large spread of values reported for the conductivity and activation energy of Cr_2O_3, which was discussed in Chapter 2.3.3. The reported conductivity and activation energy of *Park* et al. [97] were used for our calculations, as their values are very similar to the average values found in many publications [91–99].

Table 4.1: Literature values and calculated values for the conductivity and corresponding resistance of Co_3O_4 and Cr_2O_3. E_a and $\sigma_{800\,°C}$ correspond to literature values, $\sigma_{600\,°C}$ was calculated using Equation 2.20, L represents the thickness of the observed oxide layer obtained from the cross sections (Figure 4.1), and $R_{600\,°C}$ was calculated according to Equation 2.21 with the area $A = 1\,cm^2$.

	E_a (eV)	$\sigma_{800\,°C}$ (S·cm^{-1})	$\sigma_{600\,°C}$ (S·cm^{-1})	L (nm)	$R_{600\,°C}$ (mΩ)
Co_3O_4	0.79 [140]	6.7 [81]	0.94	1 200 5 700	0.13 0.60
Cr_2O_3	0.46 [97]	0.008 [97]	0.0026	40	1.56

4.2 Long-Term Exposed Ce/Co-Coated AISI 441

Two main factors are of importance for widespread commercialization of solid oxide fuel cell technology to be successfull: the long-term stability of the systems and the material cost. As mentioned in Chapter 2.3 both factors can be strongly influenced by the choice of the interconnect material in combination with the use of coatings. One strategy to reduce costs is the use of cheap commercially available steels, such as AISI 441, instead of expensive steels, such as Crofer 22 APU. However, coatings are essential to guarantee a long lifetime. Currently, one of the state-of-the art coatings is the Ce/Co coating, as mentioned in 2.3.2 and [19]. To examine the long-term stability of Ce/Co-coated (10 nm Ce + 640 nm Co) AISI 441, AB Sandvik Materials Technology exposed the steel discontinuously for up to 37 000 h at 800 °C. Subsequent analysis was carried out at Chalmers.

4.2.1 Mass Gains

Long-term (up to 37 000 h) exposed Ce/Co-coated AISI 441 exhibited near parabolic behavior (Figure 4.4). A slight deviation in mass gain between the two different batches was found. This could be due to a slight variation in the composition of the materials. The mass gain of Ce/Co-coated AISI 441 that was exposed in a tube furnace for 1 000 h was comparable to the mass gain of Ce/Co-coated AISI 441 exposed in a box furnace. However, after 3 000 h, a lower mass gain was observed for the samples exposed in a tube furnace. This can be due to the fact that the tube furnace exposure was conducted isothermally, whereas the samples exposed in the box furnace were regularly cooled down to continuously record mass gain.

4.2.2 Microstructural Investigation

The microstructural investigation of samples exposed for 7 000 h, 23 000 h, and 35 000 h showed similar results for all three time lengths (Figure 4.4). A thick thermally grown Cr_2O_3 layer was found below the oxidized Co coating. The $(Co,Mn)_3O_4$ layer of all samples was roughly between 1 - 1.5 μm, while the Cr_2O_3 layer was 5 μm thick after 7 000 h, 12 -15 μm thick after 23 000 h, and 17 - 20 μm thick after 35 000 h of exposure.

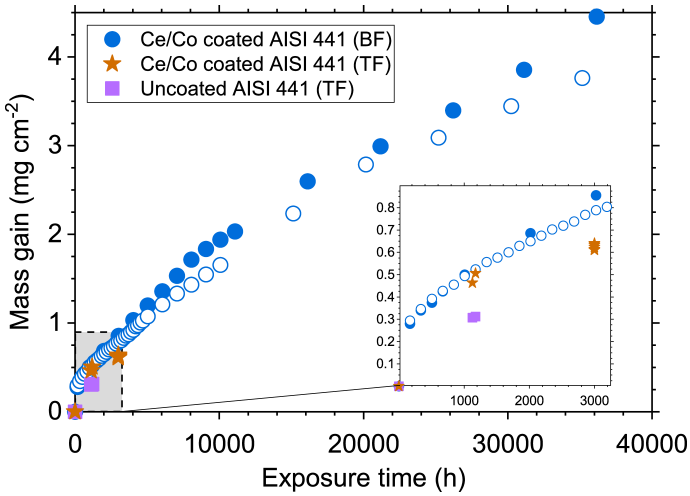

Figure 4.4: *Mass gain for AISI 441 exposed up to 37 000 h at 800 °C. Samples were exposed either in box furnaces (BF) by Sandvik Materials Technology or in tube furnaces (TF) at Chalmers. Two different batches (filled vs. open circles) were exposed for the long-term samples, and their mass gains are average values over a range of samples. The overall exposure time was 35 000 h for the batch that was used for subsequent ASR measurements (open circles), and 37 000 h for the batch that was used for subsequent Cr-evaporation measurements (filled circles).*

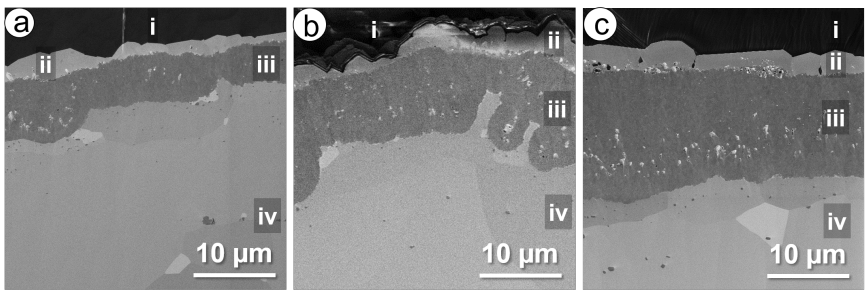

Figure 4.5: *SEM-Backscattered electron (BSE) images of BIB-milled cross sections of Ce/Co-coated 441 samples exposed at 800 °C in laboratory air. Exposure times were a) 7 000 h, b) 23 000 h and c) 35 000 h. The present layers were identified with EDX as i) Glue, ii) $(Co,Mn)_3O_4$, iii) Cr_2O_3, and iv) steel substrate.*

4.2.3 Cr-Evaporation

Cr-evaporation measurements showed relatively low Cr-evaporation rates for Ce/Co-coated AISI 441 even after 37 000 h of exposure (Figure 4.6) compared to the Cr-evaporation rate for uncoated AISI 441. Uncoated AISI 441 had an average Cr-evaporation rate of $1.8 \cdot 10^{-4}$ mg cm^{-2}h^{-1}, whereas the average Cr-evaporation rate was $9.9 \cdot 10^{-6}$ mg cm^{-2}h^{-1} for

Ce/Co-coated AISI 441 exposed in a tube furnace for 1 000 h, and $2.5 \cdot 10^{-5}$ mg cm^{-2}h^{-1} for Ce/Co-coated AISI 441 exposed in a box furnace for 37 000 h. The elevated Cr-evaporation rate after the long-term exposure compared to the short-term exposure probably had two reasons. First, the long-term exposure was carried out in stagnant laboratory air, and an accumulation of Cr in the coating can occur in this atmosphere. However, a constant humid air flow was blown over the sample during Cr-evaporation measurements, thus, leading to the evaporation of the accumulated Cr in the material. This especially can explain the decline in Cr-evaporation rate during the first two measurements (inset in Figure 4.6). Second, as mentioned in 3.2.2, the samples had to be cut down after the long-term exposure and before the Cr-evaporation measurements, which gave an unexposed and uncoated edge. This could explain the slight increase in Cr-evaporation rate.

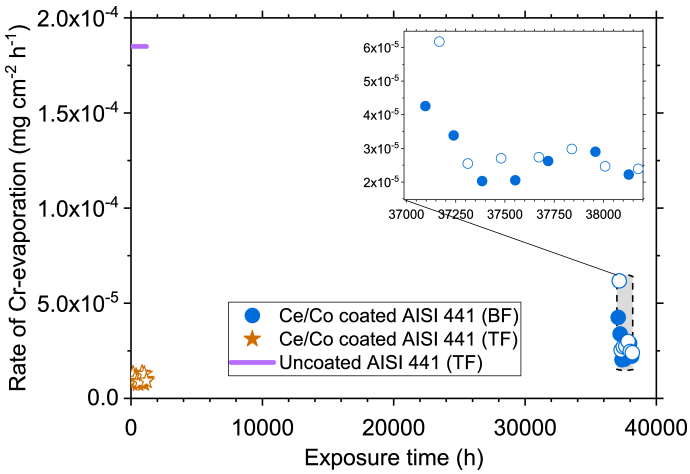

Figure 4.6: *Rate of Cr-evaporation as a function of time for AISI 441 exposed up to 38 100 h at 800 °C. Samples were exposed either in box furnaces (BF) by AB Sandvik Materials Technology or in tube furnaces (TF) at Chalmers. The Cr-evaporation measurements were all conducted in tube furnaces.*

4.2.4 Area Specific Resistance

Low ASR values were measured for long-term exposed Ce/Co-coated AISI 441 (Figure 4.7). Similar to the mass gains observed for this material, the increase in ASR values followed a parabolic trend. This is not surprising as according to Chapter 4.1 and Paper I the ASR is mainly dependent on the thermally grown Cr_2O_3 layer. However, a new question arose in view of this: according to the theoretical calculations undertaken in Table 4.1 and Equation 4.1, the ASR for a 20 μm thick Cr_2O_3 layer (on both sides of the sample) should be around 500 mΩcm^2 after 37 000 h of exposure. This discrepancy can be explained with three different approaches. First, it is possible that the Cr_2O_3 layer was doped, for example, with Fe or Mn. This would greatly impact conductivity and could

lead to much lower ASR values than expected. Second, as can be seen especially in Figure 4.5 the thickness of the Cr_2O_3 layer varies dramatically. This could lead to much lower ASR values if the electrons diffuse through the thinner part of the Cr_2O_3 layer. And finally, the oxygen partial pressure gradient that exists throughout the scale could have a beneficial effect on resistance. In the future, further analysis, such as TEM/EDX analysis or glow-discharge optical emission spectroscopy (GDOES), will hopefully answer the question if impurities are present in the Cr_2O_3 layer, while the preparation and analysis of additional cross sections will result in a better statistical overview of the thickness of the Cr_2O_3 layer and how much this deviates.

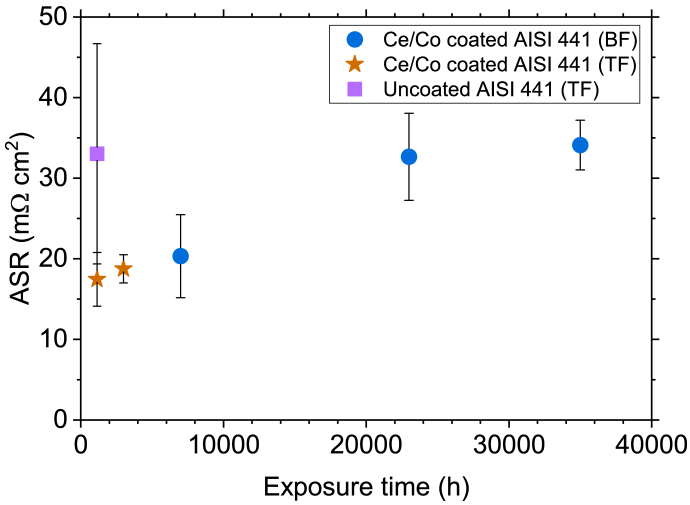

Figure 4.7: *ASR for AISI 441 exposed up to 37 000 h at 800 °C. Samples were exposed either in box furnaces (BF) by AB Sandvik Materials Technology or in tube furnaces (TF) at Chalmers. Error bars indicate standard deviations.*

In general, the low Cr-evaporation rates and the low ASR values after long-term exposure suggest that Ce/Co-coated AISI 441 shows promising long-term stability in air atmosphere at 800 °C.

4.3 Pre-oxidation and its Influence on the Dual Atmosphere Effect

As mentioned in Chapter 2.3.4, the dual atmosphere effect leads to increased corrosion on the air-facing side of uncoated AISI 441 at 600 °C in dual atmosphere compared to single atmosphere. In previous studies by *Alnegren* et al. [141], a beneficial effect of pre-oxidation was observed in dual atmosphere. This effect was examined more closely in Paper III with regard to two different parameters: the pre-oxidation time and the pre-oxidation location, i.e. pre-oxidation layer present on the fuel-facing side or on the air-facing side.

4.3.1 Influence of Pre-oxidation Time on Corrosion Behavior in Dual Atmosphere

A clear dependence of the pre-oxidation time on the corrosion resistance of uncoated AISI 441 in dual atmosphere was found (Figure 4.8). This dependence shows that longer pre-oxidation times lead to an increase in corrosion resistance. The reverse conclusion that shorter pre-oxidation times lead to an earlier onset of breakaway corrosion could, within limitations (e.g. coatings might need long pre-oxidation times), also allow for accelerated testing.

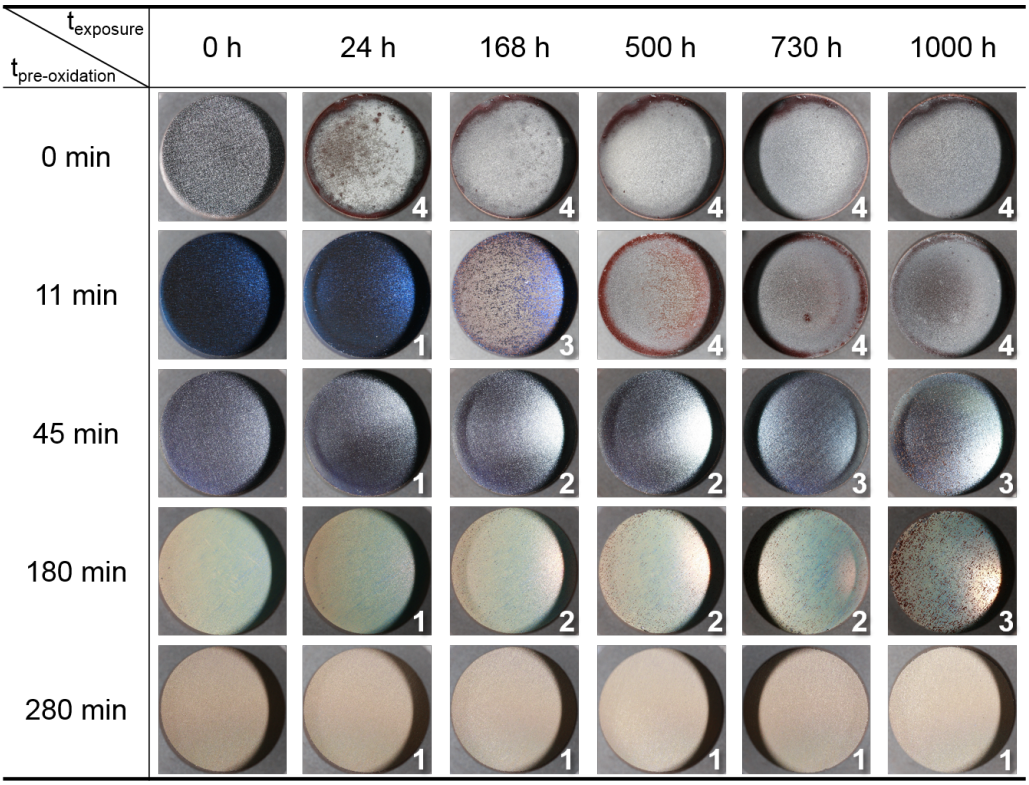

Figure 4.8: *Photographs of the air-facing side of AISI 441 taken during discontinuous dual atmosphere exposure at 600 °C. The numbers at the bottom of each picture rate the progress of corrosion. Each number is defined as follows: 1 = only protective behavior present, 2 = mostly protective behavior present, 3 = mostly corroded surface, and 4 = completely corroded surface.*

Scanning electron microscopy confirmed that longer pre-oxidation times led to an increase in corrosion resistance (Figure 4.9). Thick iron-rich oxide layers were found on the air-side of non-pre-oxidized and 11 min pre-oxidized AISI 441, whereas 45 min pre-oxidized and 180 min pre-oxidized samples showed iron-rich nodules on a protective

oxide, and 280 min pre-oxidized AISI 441 showed hardly any iron-rich oxides on the entire surface.

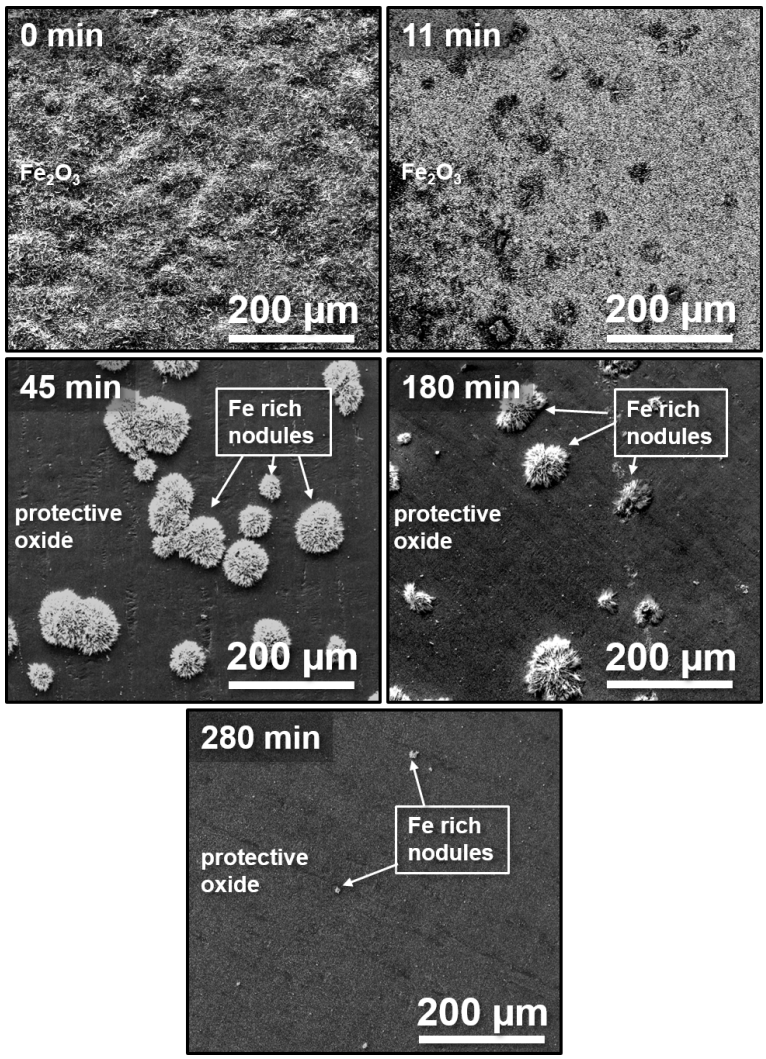

Figure 4.9: *SEM micrographs of the air-facing surface of AISI 441 exposed to dual atmosphere for 1 000 h at 600 °C. 5 different pre-oxidation times were employed: 0 min, 11 min, 45 min, 180 min, and 280 min.*

The cross section of the air-facing side of 11 min pre-oxidized AISI 441 that was exposed in dual atmosphere for 1 000 h formed a roughly 37 μm thick breakaway oxidation layer (Figure 4.10). This layer consisted of two different oxides. The top layer had a Fe:O ratio of 2:3 and, for this reason, was expected to be hematite, and the lower oxide was assumed to be a mixed $(Fe,Cr)_3O_4$ spinel. This microstructure of breakaway corrosion was

found for all pre-oxidation times regardless if the entire surface was covered by breakaway corrosion or if only small iron-rich nodules were found on the surface. More detailed microstructural investigations on the iron-rich nodules formed on the air-facing side in dual atmosphere can be found in Paper III and in [20, 21, 141]. 11 min pre-oxidized AISI 441 also formed an iron-rich oxide layer on the hydrogen-facing side (Figure 4.10). A similarly slightly thicker iron-rich oxide layer was also found on the hydrogen-facing side of the non-pre-oxidized sample. Further analysis with XRD and TEM to understand the microstructure of this iron-rich oxide layer is still needed. However, no iron rich oxide was found on the fuel-facing side of samples pre-oxidized longer than 11 min. Instead, a protective Cr-rich oxide scale was present even after 1 000 h of dual atmosphere exposure.

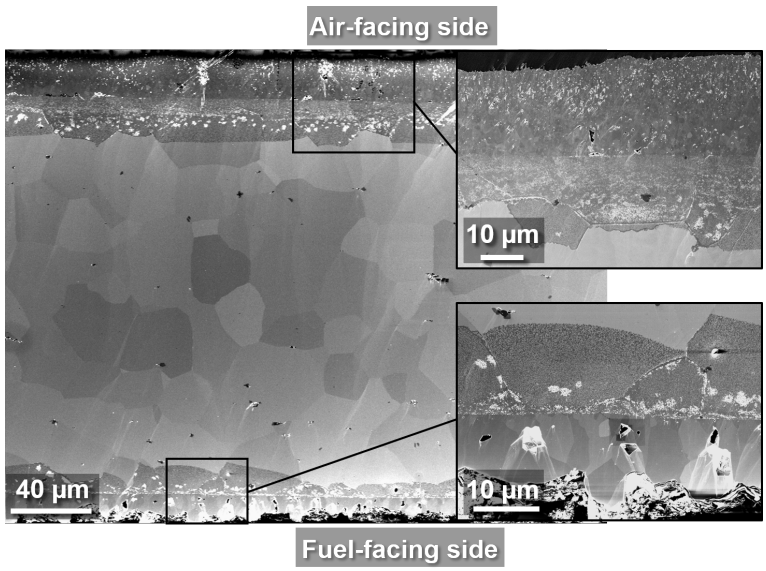

Figure 4.10: *SEM micrograph of the cross section of AISI 441 that was pre-oxidized for 11 min and, subsequently, discontinuously exposed to dual atmosphere for 1 000 h at 600 °C.*

4.3.2 Influence of Pre-oxidation Location on Corrosion Behavior in Dual Atmosphere

Two different hypotheses for the beneficial effect of pre-oxidation in dual atmosphere have been suggested. First, the formation of a protective oxide layer on the air-facing side slows down the oxidation of the alloy and, subsequently, reduces the consumption of Cr, or second, the presence of the pre-oxidation layer on the fuel-facing side slows down the ingress of hydrogen into the alloy. The results in Paper III show that the beneficial effect of pre-oxidation is mainly, if not exclusively, due to the pre-oxidation layer on the fuel-facing side (Figure 4.11 and Figure 4.12). This strongly suggests that the latter theory for the beneficial effect of pre-oxidation is true: namely, that the reduced hydrogen ingress into the alloy due to the presence of a protective oxide layer on the fuel-facing

side is the reason for the beneficial effect of pre-oxidation. This is also in agreement with studies by *Kurokawa* et al. [114, 119], who have found that hydrogen permeation through Cr_2O_3 is substantially lower than through ferritic stainless steels. Those authors reported a 94 % decrease in hydrogen permeation for a 760 nm thick oxide scale (on one side of the alloy) compared to the bare alloy. Figure 4.11 also shows that samples on which the air-facing side was ground, i.e. samples e and f, had improved corrosion resistance in dual atmosphere compared to the sample that was not ground, i.e. sample b. An effect of surface modification on corrosion behavior has previously been discussed in different studies [59, 142, 143], and a beneficial effect of grinding was specifically observed by *Niewolak* et al. [59].

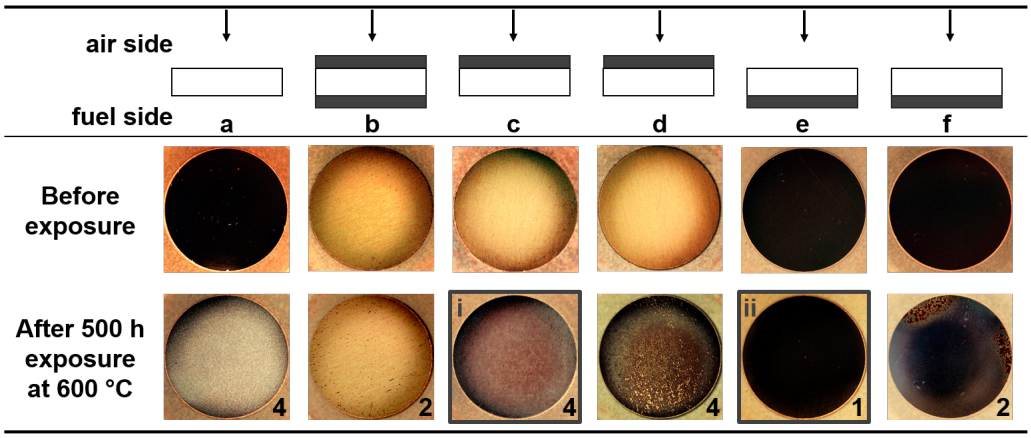

Figure 4.11: *Photographs of the air-facing side of AISI 441 exposed to dual atmosphere for 500 h at 600 °C. All samples were pre-oxidized for 180 min in air prior to exposure and, subsequently, one or two or no oxide layers were removed by grinding the sample. The letters a-f identify the different samples as follows: a) pre-oxidation removed from both sides, b) pre-oxidation layer present on both sides, c) and d) pre-oxidation layer removed from the hydrogen-facing side, and e) and f) pre-oxidation layer present on the hydrogen-facing side. The numbers at the bottom of each picture rate the progress of corrosion. Each number is defined as follows: 1 = only protective behavior present, 2 = mostly protective behavior present, 3 = mostly corroded surface, and 4 = completely corroded surface. Detailed SEM analysis was performed on the samples marked with i and ii.*

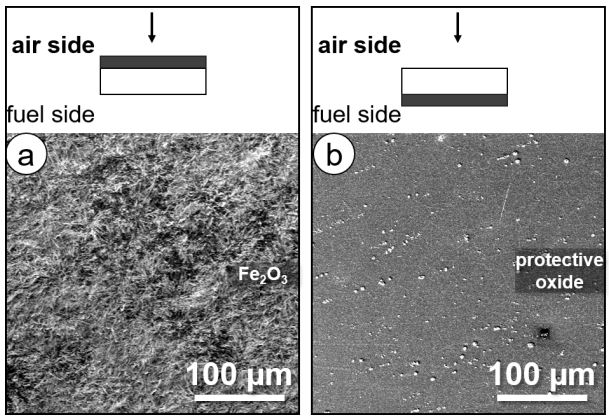

Figure 4.12: *SEM micrographs of the air-facing side of AISI 441 exposed to dual atmosphere for 500 h at 600 °C. The samples were pre-oxidized prior to exposure for 180 min in air and, subsequently, the oxide layer on either the air-facing side or the hydrogen-facing side was removed by grinding the sample. A) corresponds to the sample where the oxide layer on the hydrogen-facing side was removed, and b) corresponds to the sample where the oxide layer on the hydrogen-facing side was present.*

Chapter 5

Summary and Outlook

The degradation mechanisms of ferritic stainless steels used as interconnects in SOFCs were examined in the present work. Three different aspects were analyzed in detail:

- The influence of Co coating and thermally grown Cr_2O_3 on the overall resistance of an interconnect exposed to air atmosphere at 600 °C.
- The longevity of a Ce/Co-coated AISI 441 at 800 °C.
- The dual atmosphere effect at 600 °C with regard to the impact of a pre-oxidation step implemented prior to dual atmosphere exposure at 600 °C.

It was found that Co-coated Crofer 22 APU, which was exposed for 500 h at 600 °C, had similar ASR values between 8 and 12 $m\Omega cm^2$ regardless of the Co_3O_4 thickness. This strongly suggests that the thermally grown Cr_2O_3 layer present beneath the Co_3O_4 layer is the main factor contributing to the overall ASR values. This finding was corroborated with theoretical calculations that showed that the rather poorly conductive Cr_2O_3 was in most cases, the dominant contributor to the overall ASR. Therefore, attempts to make the spinel coating more conductive should not be the main focus of further research. Instead, the focus should be on decreasing the growth rate of Cr_2O_3. This can be achieved by adding reactive elements, such as Ce, either to the substrate material or as a coating.

Additionally, the longevity of Ce/Co-coated AISI 441 was demonstrated. This material was exposed by AB Sandvik Material Technology for up to 37 000 h at 800 °C. Cr-evaporation measurements after exposure showed that the Cr-evaporation rate of the long-term exposed samples did not differ much from the rate observed for Ce/Co-coated AISI 441, which was only exposed for 1 000 h. Furthermore, ASR measurements for samples exposed for 7 000 h, 23 000 h, and 35 000 h showed parabolic behavior and very low ASR values even after 35 000 h (ASR $\leq 40\, m\Omega cm^2$). This suggests that Ce/Co coatings are highly effective against Cr-evaporation and in reducing the growth rate of Cr_2O_3 even after an exposure for 37 000 h.

Two factors were investigated to further examine the influence of pre-oxidation on the corrosion behavior of uncoated AISI 441 in dual atmosphere at 600 °C: the length of the pre-oxidation and the location of the pre-oxidation (hydrogen side or air side). It was discovered that an increase in resistance against the dual atmosphere effect was present for longer pre-oxidation times. For example, 280 min pre-oxidized AISI 441 showed hardly any signs of corrosion after 1 000 h of dual atmosphere exposure, while quite severe corrosion was found after the same timeframe with shorter pre-oxidation times. Furthermore, it was

also demonstrated that the pre-oxidation layer on the fuel-facing side is more important for corrosion resistance in dual atmosphere than the pre-oxidation layer on the air-facing side. Both discoveries give more insight into the dual atmosphere effect: the main reason for the beneficial effect is the decrease in the dissolution of hydrogen in the steel in the presence of a pre-oxidation layer. The results suggest that thicker pre-oxidation layers on the fuel-facing side lead to a decrease in hydrogen dissolution in the steel. This is in agreement with *Kurokawa* et al. [114, 119], who have found that hydrogen permeation through Cr_2O_3 is much slower than through a ferritic stainless steel. Therefore, the results suggest that fuel-side coatings, which limit the ingress of hydrogen into the steel, might be a solution to avoid the dual atmosphere effect. The results also show that accelerated testing should be possible.

References

[1] IPCC. *Climate change 2013: the physical science basis. Contribution of working group I to the fifth assessment report of the intergovernmental panel on climate change*. Ed. by T. F. Stocker, D. Qin, G.-K. Plattner, M. M. B. Tignor, S. K. Allen, J. Boschung, A. Nauels, Y. Xia, V. Bex, and P. M. Midgley. Cambridge, United Kingdom and New York: Cambridge University Press, 2013. ISBN: 978-1-107-66182-0.

[2] S. Becker, B. A. Frew, G. B. Andresen, T. Zeyer, S. Schramm, M. Greiner, and M. Z. Jacobson. Features of a fully renewable US electricity system: optimized mixes of wind and solar PV and transmission grid extensions. *Energy* **72** (2014), 443–458. DOI: 10.1016/j.energy.2014.05.067.

[3] H. Yu, C. Hebling, and S. Revathi. "Fuel cells: microsystems". *Reference module in materials science and materials engineering*. 1st ed. Elsevier, 2016. DOI: 10.1016/B978-0-12-803581-8.01727-6.

[4] N. P. Brandon, E. Ruiz-Trejo, and P. Boldrin. *Solid oxide fuel cell lifetime and reliability: critical challenges in fuel cells*. 1st ed. Oxford: Elsevier, 2017. ISBN: 0081011024 9780081011027.

[5] M. Powell, K. Meinhardt, V. Sprenkle, L. Chick, and G. McVay. Demonstration of a highly efficient solid oxide fuel cell power system using adiabatic steam reforming and anode gas recirculation. *Journal of Power Sources* **205** (2012), 377–384. DOI: 10.1016/j.jpowsour.2012.01.098.

[6] I. Staffell, A. Ingram, and K. Kendall. Energy and carbon payback times for solid oxide fuel cell based domestic CHP. *International Journal of Hydrogen Energy* **37** (2012), 2509–2523. DOI: 10.1016/j.ijhydene.2011.10.060.

[7] A. B. Stambouli and E. Traversa. Solid oxide fuel cells (SOFCs): a review of an environmentally clean and efficient source of energy. *Renewable and Sustainable Energy Reviews* **6** (2002), 433–455. DOI: 10.1016/S1364-0321(02)00014-X.

[8] *Manufacturing cost analysis of 1 kW and 5kW solid oxide fuel cell (SOFC) for auxillary power applications*. Report. Battelle, 2014.

[9] A. Kirubakaran, S. Jain, and R. K. Nema. A review on fuel cell technologies and power electronic interface. *Renewable and Sustainable Energy Reviews* **13** (2009), 2430–2440. DOI: 10.1016/j.rser.2009.04.004.

[10] W. J. Quadakkers, J. Piron-Abellan, V. Shemet, and L. Singheiser. Metallic interconnectors for solid oxide fuel cells – a review. *Materials at High Temperatures* **20** (2003), 115–127. DOI: 10.1179/mht.2003.015.

[11] N. Shaigan, W. Qu, D. G. Ivey, and W. Chen. A review of recent progress in coatings, surface modifications and alloy developments for solid oxide fuel cell ferritic stainless steel interconnects. *Journal of Power Sources* **195** (2010), 1529–1542. DOI: 10.1016/j.jpowsour.2009.09.069.

[12] H. Kurokawa, C. P. Jacobson, L. C. DeJonghe, and S. J. Visco. Chromium vaporization of bare and of coated iron–chromium alloys at 1073 K. *Solid State Ionics* **178** (2007), 287–296. DOI: 10.1016/j.ssi.2006.12.010.

[13] R. Trebbels, T. Markus, and L. Singheiser. Investigation of chromium vaporization from interconnector steels with spinel coatings. *Journal of The Electrochemical Society* **157** (2010), B490–B495. DOI: 10.1149/1.3298434.

[14] J. Froitzheim and J. E. Svensson. Multifunctional nano-coatings for SOFC interconnects. *ECS Transactions* **35** (2011), 2503–2508. DOI: 10.1149/1.3570248.

[15] N. Birks, G. H. Meier, and F. S. Pettit. *Introduction to the high-temperature oxidation of metals*. 2nd ed. Cambridge: Cambridge University Press, 2006.

[16] P. Y. Hou and J. Stringer. The effect of reactive element additions on the selective oxidation, growth and adhesion of chromia scales. *Materials Science and Engineering: A* **202** (1995), 1–10. DOI: 10.1016/0921-5093(95)09798-8.

[17] Z. Yang, M. S. Walker, P. Singh, J. W. Stevenson, and T. Norby. Oxidation behavior of ferritic stainless steels under SOFC interconnect exposure conditions. *Journal of the Electrochemical Society* **151** (2004), B669–B678. DOI: 10.1149/1.1810393.

[18] G. Chen, X. Xin, T. Luo, L. Liu, Y. Zhou, C. Yuan, C. Lin, Z. Zhan, and S. Wang. $Mn_{1.4}Co_{1.4}Cu_{0.2}O_4$ spinel protective coating on ferritic stainless steels for solid oxide fuel cell interconnect applications. *Journal of Power Sources* **278** (2015), 230–234. DOI: 10.1016/j.jpowsour.2014.12.070.

[19] M. Galvez Sanchez, M. Oum, S. Pandyian, A. J. Majewski, L. Troskialina, and R. Steinberger-Wilckens. *Scored 2:0 - Steel coatings for reducing degradation*. Report. University of Birmingham, 2017.

[20] P. Alnegren, M. Sattari, J.-E. Svensson, and J. Froitzheim. Severe dual atmosphere effect at 600 °C for stainless steel 441. *Journal of Power Sources* **301** (2016), 170–178. DOI: 10.1016/j.jpowsour.2015.10.001.

[21] P. Alnegren, M. Sattari, J.-E. Svensson, and J. Froitzheim. Temperature dependence of corrosion of ferritic stainless steel in dual atmosphere at 600–800 °C. *Journal of Power Sources* **392** (2018), 129–138. DOI: 10.1016/j.jpowsour.2018.04.088.

[22] R. Steinberger-Wilckens. "Introduction to fuel cell basics". *Advances in medium and high temperature solid oxide fuel cell technology*. Ed. by M. Boaro and A. Salvatore Aricò. 1st ed. CISM International Centre for Mechanical Sciences, 2017. DOI: 10.1007/978-3-319-46146-5.

[23] J. Larminie and A. Dicks. *Fuel cell systems explained*. 2nd ed. West Sussex: John Wiley & Sons Ltd, 2003. DOI: 10.1002/9781118878330.

[24] S. C. Singhal. "Solid oxide fuel cells: past, present and future". *Solid oxide fuels cells: facts and figures: past present and future perspectives for SOFC technologies*. Ed. by J. T. S. Irvine and P. Connor. 1st ed. London: Springer London, 2013, pp. 1–23. DOI: 10.1007/978-1-4471-4456-4_1.

[25] S. C. Singhal and K. Kendall. "Introduction to SOFCs". *High temperature solid oxide fuel cells - fundamentals, design and applications*. Ed. by S. C. Singhal and K. Kendall. 1st ed. Oxford: Elsevier, 2003. ISBN: 978-1-8561-7387-2.

[26] T. Taner. Energy and exergy analyze of PEM fuel cell: a case study of modeling and simulations. *Energy* **143** (2018), 284–294. DOI: 10.1016/j.energy.2017.10.102.

[27] K. Lee, S. Kang, and K.-Y. Ahn. Development of a highly efficient solid oxide fuel cell system. *Applied Energy* **205** (2017), 822–833. DOI: 10.1016/j.apenergy.2017.08.070.

[28] W. Winkler. "Thermodynamics". *High temperature solid oxide fuel cells - fundamentals, design and applications*. Ed. by S. C. Singhal and K. Kendall. 1st ed. Oxford: Elsevier, 2003. ISBN: 978-1-8561-7387-2.

[29] T. Ishihara, N. M. Sammes, and O. Yamamoto. "Electrolytes". *High temperature solid oxide fuel cells - fundamentals, design and applications*. Ed. by S. C. Singhal and K. Kendall. 1st ed. Oxford: Elsevier, 2003. ISBN: 978-1-8561-7387-2.

[30] C. Xia. "Electrolytes". *Solid oxide fuel cells: materials properties and performance*. Ed. by J. W. Fergus, R. Hui, X. Li, D. P. Wilkinson, and J. Zhang. 1st ed. Florida: Taylor & Francis Group, 2009.

[31] K. T. Lee, H. S. Yoon, and E. D. Wachsman. The evolution of low temperature solid oxide fuel cells. *Journal of Materials Research* **27** (2012), 2063–2078. DOI: 10.1557/jmr.2012.194.

[32] E. D. Wachsman and K. T. Lee. Lowering the temperature of solid oxide fuel cells. *Science* **334** (2011), 935–939. DOI: 10.1126/science.1204090.

[33] A. McEvoy. "Anodes". *High temperature solid oxide fuel cells - fundamentals, design and applications*. Ed. by S. C. Singhal and K. Kendall. 1st ed. Oxford: Elsevier, 2003. ISBN: 978-1-8561-7387-2.

[34] H. S. Spacil. *Fuel cell comprising a stabilized zirconium oxide electrolyte and a doped indium or tin oxide cathode*. Patent. 1970.

[35] Z. Cheng, J.-H. Wang, and M. Liu. "Anodes". *Solid oxide fuel cells: materials properties and performance*. Ed. by J. W. Fergus, R. Hui, X. Li, D. P. Wilkinson, and J. Zhang. 1st ed. Florida: Taylor & Francis Group, 2009.

[36] H. Yokokawa and T. Horita. "Cathodes". *High temperature solid oxide fuel cells - fundamentals, design and applications*. Ed. by S. C. Singhal and K. Kendall. 1st ed. Oxford: Elsevier, 2003. ISBN: 978-1-8561-7387-2.

[37] C.-C. T. Yang, W.-C. J. Wei, and A. Roosen. Electrical conductivity and microstructures of $La_{0.65}Sr_{0.3}MnO_3$–8mol% yttria-stabilized zirconia. *Materials Chemistry and Physics* **81** (2003), 134–142. DOI: 10.1016/S0254-0584(03)00158-5.

[38] Y. Ji, J. A. Kilner, and M. F. Carolan. Electrical properties and oxygen diffusion in yttria-stabilised zirconia (YSZ)–$La_{0.8}Sr_{0.2}MnO_{3\pm\delta}$ (LSM) composites. *Solid State Ionics* **176** (2005), 937–943. DOI: 10.1016/j.ssi.2004.11.019.

[39] S. P. Jiang and J. Li. "Cathodes". *Solid oxide fuel cells: materials properties and performance*. Ed. by J. W. Fergus, R. Hui, X. Li, D. P. Wilkinson, and J. Zhang. 1st ed. Florida: Taylor & Francis Group, 2009.

[40] Z. Yang and J. W. Fergus. "Interconnects". *Solid oxide fuel cells: materials properties and performance*. Ed. by J. W. Fergus, R. Hui, X. Li, D. P. Wilkinson, and J. Zhang. 1st ed. Florida: Taylor & Francis Group, 2009.

[41] A. Brouzgou, A. Demin, and P. Tsiakaras. "Interconnects for solid oxide fuel cells". *Advances in medium and high temperature Solid Oxide Fuel Cell Technology*. Ed. by M. Boaro and A. A. Salvatore. 1st ed. Cham: Springer International Publishing, 2017, pp. 119–153. DOI: 10.1007/978-3-319-46146-5_4.

[42] H. U. Anderson and F. Tietz. "Interconnects". *High temperature solid oxide fuel cells - fundamentals, design and applications*. Ed. by S. C. Singhal and K. Kendall. 1st ed. Oxford: Elsevier, 2003. ISBN: 978-1-8561-7387-2.

[43] P. Kofstad. *High temperature corrosion*. 1st ed. London and New York: Elsevier Applied Science Publishers Ltd., 1988. ISBN: 1-85166-154-9.

[44] D. J. Young. *High temperature oxidation and corrosion of metals*. 2nd ed. Elsevier Ltd., 2016. DOI: 10.1016/B978-0-08-100101-1.00002-9.

[45] H. J. T. Ellingham. Reducibility of oxides and sulphides in metallurgical processes. *Journal of the Society of Chemical Industry* **63** (1944), 125–160. DOI: 10.1002/jctb.5000630501.

[46] C. Wagner. Beitrag zur theorie des anlaufvorgangs. *Zeitschrift für Physikalische Chemie* **21B** (1933), 25. DOI: 10.1515/zpch-1933-2105.

[47] H. E. Evans, A. T. Donaldson, and T. C. Gilmour. Mechanisms of breakaway oxidation and application to a chromia-forming steel. *Oxidation of Metals* **52** (1999), 379–402. DOI: 10.1023/a:1018855914737.

[48] M. Schütze, D. Renusch, and M. Schorr. Chemical-mechanical failure of oxide scales on 9% Cr steels in air with H_2O. *Materials at High Temperatures* **22** (2005), 113–120. DOI: 10.1179/mht.2005.013.

[49] E. Essuman, G. H. Meier, J. Żurek, M. Hänsel, L. Singheiser, and W. J. Quadakkers. Enhanced internal oxidation as trigger for breakaway oxidation of Fe–Cr alloys in gases containing water vapor. *Scripta Materialia* **57** (2007), 845–848. DOI: 10.1016/j.scriptamat.2007.06.058.

[50] G. Hultquist, B. Tveten, and E. Hörnlund. Hydrogen in chromium: influence on the high-temperature oxidation kinetics in H_2O, oxide-growth mechanisms, and scale adherence. *Oxidation of Metals* **54** (2000), 1–10. DOI: 10.1023/a:1004610626903.

[51] L. Luo, M. Su, P. Yan, L. Zou, D. K. Schreiber, D. R. Baer, Z. Zhu, G. Zhou, Y. Wang, S. M. Bruemmer, Z. Xu, and C. Wang. Atomic origins of water-vapour-promoted alloy oxidation. *Nature Materials* **17** (2018), 514–518. DOI: 10.1038/s41563-018-0078-5.

[52] J. Zurek, D. J. Young, E. Essuman, M. Hänsel, H. J. Penkalla, L. Niewolak, and W. J. Quadakkers. Growth and adherence of chromia based surface scales on Ni-base alloys in high- and low-pO_2 gases. *Materials Science and Engineering: A* **477** (2008), 259–270. DOI: 10.1016/j.msea.2007.05.035.

[53] S. Henry, J. Mougin, Y. Wouters, J. P. Petit, and A. Galerie. Characterization of chromia scales grown on pure chromium in different oxidizing atmospheres. *Materials at High Temperatures* **17** (2000), 231–234. DOI: 10.1179/mht.2000.17.2.008.

[54] N. B. Pilling and R. E. Bedworth. The oxidation of metals at high temperatures. *Journal of the Institute of Metals* **29** (1923), 529–582.

[55] E. McCafferty. *Introduction to corrosion science*. 1st ed. New York: Springer, 2010. DOI: 10.1007/978-1-4419-0455-3.

[56] B. B. Ebbinghaus. Thermodynamics of gas phase chromium species: the chromium oxides, the chromium oxyhydroxides, and volatility calculations in waste incineration processes. *Combustion and Flame* **93** (1993), 119–137. DOI: 10.1016/0010-2180(93)90087-J.

[57] K. Hilpert, D. Das, M. Miller, D. H. Peck, and R. Weiß. Chromium vapor species over solid oxide fuel cell interconnect materials and their potential for degradation processes. *Journal of The Electrochemical Society* **143** (1996), 3642–3647. DOI: 10.1149/1.1837264.

[58] E. J. Opila, D. L. Myers, N. S. Jacobson, I. M. B. Nielsen, D. F. Johnson, J. K. Olminsky, and M. D. Allendorf. Theoretical and experimental investigation of the hermochemistry of $CrO_2(OH)_2(g)$. *The Journal of Physical Chemistry A* **111** (2007), 1971–1980. DOI: 10.1021/jp0647380.

[59] L. Niewolak, E. Wessel, L. Singheiser, and W. J. Quadakkers. Potential suitability of ferritic and austenitic steels as interconnect materials for solid oxide fuel cells operating at 600 °C. *Journal of Power Sources* **195** (2010), 7600–7608. DOI: 10.1016/j.jpowsour.2010.06.007.

[60] L. Niewolak, F. Tietz, and W. J. Quadakkers. "Interconnects". *High-temperature solid oxide fuel cells for the 21st century: fundamentals, design and applications*. 2nd ed. 2015. DOI: 10.1016/B978-0-12-410453-2.00007-5.

[61] R. Sachitanand, M. Sattari, J.-E. Svensson, and J. Froitzheim. Evaluation of the oxidation and Cr evaporation properties of selected FeCr alloys used as SOFC interconnects. *International Journal of Hydrogen Energy* **38** (2013), 15328–15334. DOI: 10.1016/j.ijhydene.2013.09.044.

[62] J. Fergus and Y. Zhao. Low-chromium alloys for solid oxide fuel cell interconnects. *ECS Transactions* **35** (2011), 2447–2453. DOI: 10.1149/1.3570242.

[63] M. R. Ardigo, I. Popa, S. Chevalier, S. Weber, O. Heintz, and M. Vilasi. Effect of water vapor on the oxidation mechanisms of a commercial stainless steel for interconnect application in high temperature water vapor electrolysis. *Oxidation of Metals* **79** (2013), 495–505. DOI: 10.1007/s11085-012-9338-y.

[64] Z. Yang, G.-G. Xia, C.-M. Wang, Z. Nie, J. Templeton, J. W. Stevenson, and P. Singh. Investigation of iron–chromium–niobium–titanium ferritic stainless steel for solid oxide fuel cell interconnect applications. *Journal of Power Sources* **183** (2008), 660–667. DOI: 10.1016/j.jpowsour.2008.05.037.

[65] W. Qu, L. Jian, D. G. Ivey, and J. M. Hill. Yttrium, cobalt and yttrium/cobalt oxide coatings on ferritic stainless steels for SOFC interconnects. *Journal of Power Sources* **157** (2006), 335–350. DOI: 10.1016/j.jpowsour.2005.07.052.

[66] J. G. Grolig, J. Froitzheim, and J.-E. Svensson. Coated stainless steel 441 as interconnect material for solid oxide fuel cells: oxidation performance and chromium evaporation. *Journal of Power Sources* **248** (2014), 1007–1013. DOI: 10.1016/j.jpowsour.2013.08.089.

[67] J. G. Grolig, J. Froitzheim, and J.-E. Svensson. Coated stainless steel 441 as interconnect material for solid oxide fuel cells: evolution of electrical properties. *Journal of Power Sources* **284** (2015), 321–327. DOI: 10.1016/j.jpowsour.2015.03.029.

[68] F. Cheng, J. Cui, L. Wang, S. Li, and J. Sun. Performance of CoNiO spinel oxide coating on AISI 430 stainless steel as interconnect for intermediate temperature solid oxide fuel cell. *International Journal of Hydrogen Energy* **42** (2017), 12477–12484. DOI: 10.1016/j.ijhydene.2017.03.217.

[69] N. Hosseini, M. H. Abbasi, F. Karimzadeh, and G. M. Choi. Development of $Cu_{1.3}Mn_{1.7}O_4$ spinel coating on ferritic stainless steel for solid oxide fuel cell interconnects. *Journal of Power Sources* **273** (2015), 1073–1083. DOI: 10.1016/j.jpowsour.2014.10.017.

[70] N. Shaigan, D. G. Ivey, and W. Chen. Metal–oxide scale interfacial imperfections and performance of stainless steels utilized as interconnects in solid oxide fuel cells. *Journal of The Electrochemical Society* **156** (2009), B765–B770. DOI: 10.1149/1.3116252.

[71] M. Stanislowski, E. Wessel, K. Hilpert, T. Markus, and L. Singheiser. Chromium vaporization from high-temperature alloys: I. Chromia-forming steels and the influence of outer oxide layers. *Journal of The Electrochemical Society* **154** (2007), A295–A306. DOI: 10.1149/1.2434690.

[72] M. Stanislowski, J. Froitzheim, L. Niewolak, W. J. Quadakkers, K. Hilpert, T. Markus, and L. Singheiser. Reduction of chromium vaporization from SOFC interconnectors by highly effective coatings. *Journal of Power Sources* **164** (2007), 578–589. DOI: 10.1016/j.jpowsour.2006.08.013.

[73] J. Froitzheim, G. H. Meier, L. Niewolak, P. J. Ennis, H. Hattendorf, L. Singheiser, and W. J. Quadakkers. Development of high strength ferritic steel for interconnect application in SOFCs. *Journal of Power Sources* **178** (2008), 163–173. DOI: 10.1016/j.jpowsour.2007.12.028.

[74] K. Yamamoto, Y. Kimura, F.-G. Wei, and Y. Mishima. Design of Laves phase strengthened ferritic heat resisting steels in the Fe–Cr–Nb(–Ni) system. *Materials Science and Engineering: A* **329-331** (2002), 249–254. DOI: 10.1016/S0921-5093(01)01586-6.

[75] H. Falk-Windisch, P. Malmberg, M. Sattari, J.-E. Svensson, and J. Froitzheim. Determination of the oxide scale growth mechanism using 18O-tracer experiments in combination with transmission electron microscopy and nanoscale secondary ion mass spectrometry. *Materials Characterization* **136** (2018), 128–133. DOI: 10.1016/j.matchar.2017.12.001.

[76] W. J. Quadakkers, H. Holzbrecher, K. G. Briefs, and H. Beske. Differences in growth mechanisms of oxide scales formed on ODS and conventional wrought alloys. *Oxidation of Metals* **32** (1989), 67–88. DOI: 10.1007/bf00665269.

[77] C. M. Cotell, G. J. Yurek, R. J. Hussey, D. F. Mitchell, and M. J. Graham. The influence of implanted yttrium on the mechanism of growth of Cr_2O_3 on Cr. *Journal of The Electrochemical Society* **134** (1987), 1871–1872. DOI: 10.1149/1.2100775.

[78] D. Naumenko, B. A. Pint, and W. J. Quadakkers. Current thoughts on reactive element effects in alumina-forming systems: in memory of John Stringer. *Oxidation of Metals* **86** (2016), 1–43. DOI: 10.1007/s11085-016-9625-0.

[79] W. J. Quadakkers, H. Greiner, M. Hänsel, A. Pattanaik, A. S. Khanna, and W. Malléner. Compatibility of perovskite contact layers between cathode and metallic interconnector plates of SOFCs. *Solid State Ionics* **91** (1996), 55–67. DOI: 10.1016/S0167-2738(96)00425-0.

[80] J. C. W. Mah, A. Muchtar, M. R. Somalu, and M. J. Ghazali. Metallic interconnects for solid oxide fuel cell: a review on protective coating and deposition techniques.

International Journal of Hydrogen Energy **42** (2016), 9219–9229. DOI: 10.1016/j.ijhydene.2016.03.195.

[81] A. Petric and H. Ling. Electrical conductivity and thermal expansion of spinels at elevated temperatures. *Journal of the American Ceramic Society* **90** (2007), 1515–1520. DOI: 10.1111/j.1551-2916.2007.01522.x.

[82] S.-I. Lee, J. Hong, H. Kim, J.-W. Son, J.-H. Lee, B.-K. Kim, H.-W. Lee, and K. J. Yoon. Highly dense Mn-Co spinel coating for protection of metallic interconnect of solid oxide fuel cells. *Journal of The Electrochemical Society* **161** (2014), F1389–F1394. DOI: 10.1149/2.0541414jes.

[83] Å. H. Persson, L. Mikkelsen, P. V. Hendriksen, and M. A. J. Somers. Interaction mechanisms between slurry coatings and solid oxide fuel cell interconnect alloys during high temperature oxidation. *Journal of Alloys and Compounds* **521** (2012), 16–29. DOI: 10.1016/j.jallcom.2011.12.095.

[84] M. Mirzaei, A. Simchi, M. A. Faghihi-Sani, and A. Yazdanyar. Electrophoretic deposition and sintering of a nanostructured manganese–cobalt spinel coating for solid oxide fuel cell interconnects. *Ceramics International* **42** (2016), 6648–6656. DOI: 10.1016/j.ceramint.2016.01.012.

[85] J. Froitzheim, S. Canovic, M. Nikumaa, R. Sachitanand, L. G. Johansson, and J. E. Svensson. Long term study of Cr evaporation and high temperature corrosion behaviour of Co coated ferritic steel for solid oxide fuel cell interconnects. *Journal of Power Sources* **220** (2012), 217–227. DOI: 10.1016/j.jpowsour.2012.06.092.

[86] X. Deng, P. Wei, M. R. Bateni, and A. Petric. Cobalt plating of high temperature stainless steel interconnects. *Journal of Power Sources* **160** (2006), 1225–1229. DOI: 10.1016/j.jpowsour.2006.03.024.

[87] H. Falk-Windisch, J. Claquesin, M. Sattari, J.-E. Svensson, and J. Froitzheim. Co- and Ce/Co-coated ferritic stainless steel as interconnect material for intermediate temperature solid oxide fuel cells. *Journal of Power Sources* **343** (2017), 1–10. DOI: 10.1016/j.jpowsour.2017.01.045.

[88] H. Falk-Windisch, M. Sattari, J.-E. Svensson, and J. Froitzheim. Chromium vaporization from mechanically deformed pre-coated interconnects in solid oxide fuel cells. *Journal of Power Sources* **297** (2015), 217–223. DOI: 10.1016/j.jpowsour.2015.07.085.

[89] K. Huang, P. Y. Hou, and J. B. Goodenough. Reduced area specific resistance for iron-based metallic interconnects by surface oxide coatings. *Materials Research Bulletin* **36** (2001), 81–95. DOI: 10.1016/S0025-5408(01)00506-2.

[90] A. Holt and P. Kofstad. Electrical-conductivity and defect structure of Cr_2O_3. I. High temperatures ($>\sim$1000 °C). *Solid State Ionics* **69** (1994), 127–136. DOI: 10.1016/0167-2738(94)90401-4.

[91] A. Holt and P. Kofstad. Electrical conductivity and defect structure of Cr_2O_3. II. Reduced temperatures ($<\sim$1000 °C). *Solid State Ionics* **69** (1994), 137–143. DOI: 10.1016/0167-2738(94)90402-2.

[92] J. G. Grolig. "Coated ferritic stainless steels as interconnects in solid oxide fuel cells". Thesis. 2015.

[93] P. Huczkowski, N. Christiansen, V. Shemet, L. Niewolak, J. Piron-Abellan, L. Singheiser, and W. J. Quadakkers. Growth mechanisms and electrical conductivity

of oxide scales on ferritic steels proposed as interconnect materials for SOFC's. *Fuel Cells* **6** (2006), 93–99. DOI: 10.1002/fuce.200500110.

[94] J. A. Crawford and R. W. Vest. Electrical conductivity of single-crystal Cr_2O_3. *Journal of Applied Physics* **35** (1964), 2413–2418. DOI: 10.1063/1.1702871.

[95] W. C. Hagel and A. U. Seybolt. Cation diffusion in Cr_2O_3. *Journal of The Electrochemical Society* **108** (1961), 1146–1152. DOI: 10.1149/1.2427973.

[96] H. Nagai, T. Fujikawa, and K.-i. Shoji. Electrical conductivity of Cr_2O_3 doped with La_2O_3, Y_2O_3 and NiO. *Transactions of the Japan Institute of Metals* **24** (1983), 581–588. DOI: 10.2320/matertrans1960.24.581.

[97] J. H. Park and K. Natesan. Electronic transport in thermally grown Cr_2O_3. *Oxidation of Metals* **33** (1990), 31–54. DOI: 10.1007/BF00665668.

[98] K. Huang, P. Y. Hou, and J. B. Goodenough. Characterization of iron-based alloy interconnects for reduced temperature solid oxide fuel cells. *Solid State Ionics* **129** (2000), 237–250. DOI: 10.1016/S0167-2738(99)00329-X.

[99] Y. Larring, R. Haugsrud, and T. Norby. HT corrosion of a Cr-5 wt% Fe-1 wt% Y_2O_3 alloy and conductivity of the oxide scale. Effects of water vapor. *Journal of the Electrochemical Society* **150** (2003), B374–B379. DOI: 10.1149/1.1587726.

[100] L. Latu-Romain, Y. Parsa, S. Mathieu, M. Vilasi, and Y. Wouters. Chromia scale thermally grown on pure chromium under controlled $p(O_2)$ atmosphere: I. Spallation investigation using photoelectrochemical techniques at a mesoscale. *Oxidation of Metals* **90** (2018), 255–266. DOI: 10.1007/s11085-018-9844-7.

[101] L. Latu-Romain, S. Mathieu, M. Vilasi, G. Renou, S. Coindeau, A. Galerie, and Y. Wouters. The role of oxygen partial pressure on the nature of the oxide scale on a NiCr model alloy. *Oxidation of Metals* **88** (2017), 481–493. DOI: 10.1007/s11085-016-9670-8.

[102] L. Latu-Romain, Y. Parsa, S. Mathieu, M. Vilasi, A. Galerie, and Y. Wouters. Towards the growth of stoichiometric chromia on pure chromium by the control of temperature and oxygen partial pressure. *Corrosion Science* **126** (2017), 238–246. DOI: 10.1016/j.corsci.2017.07.005.

[103] L. Latu-Romain, Y. Parsa, S. Mathieu, M. Vilasi, M. Ollivier, A. Galerie, and Y. Wouters. Duplex n- and p-type chromia grown on pure chromium: a photoelectrochemical and microscopic study. *Oxidation of Metals* **86** (2016), 497–509. DOI: 10.1007/s11085-016-9648-6.

[104] A. Holt and P. Kofstad. Electrical conductivity and defect structure of Mg-doped Cr_2O_3. *Solid State Ionics* **100** (1997), 201–209. DOI: 10.1016/S0167-2738(97)00352-4.

[105] A. Holt and P. Kofstad. Electrical conductivity of Cr_2O_3 doped with TiO_2. *Solid State Ionics* **117** (1999), 21–25. DOI: 10.1016/S0167-2738(98)00244-6.

[106] T. Horita, Y. Xiong, H. Kishimoto, K. Yamaji, N. Sakai, M. Brito, and H. Yokokawa. "Oxide scale formation on alloy interconnects in CH_4 fuels for solid oxide fuel cells". *Solid Oxide Fuel Cells IX*. Ed. by S. C. Singhal and J. Mizusaki. The Electrochemistry Society, pp. 1822–1831.

[107] A. Navrotsky and O. J. Kleppa. The thermodynamics of cation distributions in simple spinels. *Journal of Inorganic and Nuclear Chemistry* **29** (1967), 2701–2714. DOI: 10.1016/0022-1902(67)80008-3.

[108] Z. Lu, J. Zhu, E. A. Payzant, and M. P. Paranthaman. Electrical conductivity of the manganese chromite spinel solid solution. *Journal of the American Ceramic Society* **88** (2005), 1050–1053. DOI: 10.1111/j.1551-2916.2005.00205.x.

[109] N. Sakai, T. Horita, Y. P. Xiong, K. Yamaji, H. Kishimoto, M. E. Brito, H. Yokokawa, and T. Maruyama. Structure and transport property of manganese–chromium– iron oxide as a main compound in oxide scales of alloy interconnects for SOFCs. *Solid State Ionics* **176** (2005), 681–686. DOI: 10.1016/j.ssi.2004.11.012.

[110] A. W. Bredvei Skilbred and R. Haugsrud. The effect of dual atmosphere conditions on the corrosion of Sandvik Sanergy HT. *International Journal of Hydrogen Energy* **37** (2012), 8095–8101. DOI: 10.1016/j.ijhydene.2011.10.096.

[111] J. Rufner, P. Gannon, P. White, M. Deibert, S. Teintze, R. Smith, and H. Chen. Oxidation behavior of stainless steel 430 and 441 at 800 °C in single (air/air) and dual atmosphere (air/hydrogen) exposures. *International Journal of Hydrogen Energy* **33** (2008), 1392–1398. DOI: 10.1016/j.ijhydene.2007.12.067.

[112] P. Gannon and R. Amendola. High-temperature, dual-atmosphere corrosion of solid-oxide fuel cell interconnects. *The Journal of The Minerals, Metals & Materials Society* **64** (2012), 1470–1476. DOI: 10.1007/s11837-012-0473-3.

[113] Y. Zhao and J. Fergus. High temperature oxidation behavior of stainless steel 441 in dual atmosphere - effects of flow rate and humidity. *ECS Transactions* **16** (2009), 57–64. DOI: 10.1149/1.3224744.

[114] H. Kurokawa, K. Kawamura, and T. Maruyama. Oxidation behavior of Fe–16Cr alloy interconnect for SOFC under hydrogen potential gradient. *Solid State Ionics* **168** (2004), 13–21. DOI: 10.1016/j.ssi.2004.02.008.

[115] D. J. Young, J. Zurek, L. Singheiser, and W. J. Quadakkers. Temperature dependence of oxide scale formation on high-Cr ferritic steels in Ar–H_2–H_2O. *Corrosion Science* **53** (2011), 2131–2141. DOI: 10.1016/j.corsci.2011.02.031.

[116] J. Żurek, E. Wessel, L. Niewolak, F. Schmitz, T. U. Kern, L. Singheiser, and W. J. Quadakkers. Anomalous temperature dependence of oxidation kinetics during steam oxidation of ferritic steels in the temperature range 550–650 °C. *Corrosion Science* **46** (2004), 2301–2317. DOI: 10.1016/j.corsci.2004.01.010.

[117] L. Sánchez, M. P. Hierro, and F. J. Pérez. Effect of chromium content on the oxidation behaviour of ferritic steels for applications in steam atmospheres at high temperatures. *Oxidation of Metals* **71** (2009), 173. DOI: 10.1007/s11085-008-9134-x.

[118] S. K. Yen and Y. C. Tsai. Critical hydrogen concentration for the brittle fracture of AISI 430 stainless steel. *Journal of The Electrochemical Society* **143** (1996), 2736–2741. DOI: 10.1149/1.1837100.

[119] H. Kurokawa, Y. Oyama, K. Kawamura, and T. Maruyama. Hydrogen permeation through Fe-16Cr alloy interconnect in atmosphere simulating SOFC at 1073 K. *Journal of The Electrochemical Society* **151** (2004), A1264–A1268. DOI: 10.1149/1.1767349.

[120] Z. Yang, M. S. Walker, P. Singh, and J. W. Stevenson. Anomalous corrosion behavior of stainless steels under SOFC interconnect exposure conditions. *Electrochemical and Solid-State Letters* **6** (2003), B35–B37. DOI: 10.1149/1.1603012.

[121] B. Tveten, G. Hultquist, and T. Norby. Hydrogen in chromium: influence on the high-temperature oxidation kinetics in O_2, oxide-growth mechanisms, and scale adherence. *Oxidation of Metals* **51** (1999), 221–233. DOI: 10.1023/a:1018866505708.

[122] G. R. Holcomb, M. Ziomek-Moroz, S. D. Cramer, B. S. Covino, and S. J. Bullard. Dual-environment effects on the oxidation of metallic interconnects. *Journal of Materials Engineering and Performance* **15** (2006), 404–409. DOI: 10.1361/105994906x117198.

[123] H. Falk-Windisch, J. Claquesin, J.-E. Svensson, and J. Froitzheim. The effect of metallic Co-coating thickness on ferritic stainless steels intended for use as interconnect material in intermediate temperature solid oxide fuel cells. *Oxidation of Metals* **89** (2018), 233–250. DOI: 10.1007/s11085-017-9782-9.

[124] J. Froitzheim, H. Ravash, E. Larsson, L. G. Johansson, and J.-E. Svensson. Investigation of chromium volatilization from FeCr interconnects by a denuder technique. *Journal of The Electrochemical Society* **157** (2010), B1295. DOI: 10.1149/1.3462987.

[125] R. Faust. "Dual atmosphere corrosion of ferritic stainless steel used for solid oxide fuel cell applications - The importance of the location of pr-oxidation scales". Thesis. 2017.

[126] M.-C. Fournier-Salaün and P. Salaün. Quantitative determination of hexavalent chromium in aqueous solutions by UV-Vis spectrophotometer. *Central European Journal of Chemistry* **5** (2007), 1084–1093. DOI: 10.2478/s11532-007-0038-4.

[127] E. Moore and L. Smart. *Solid state chemistry: an introduction*. 3rd ed. Boca Raton: CRC Taylor & Francis, 2005. ISBN: 0-203-49635-3.

[128] K. L. Scrivener. Backscattered electron imaging of cementitious microstructures: understanding and quantification. *Cement and Concrete Composites* **26** (2004), 935–945. DOI: 10.1016/j.cemconcomp.2004.02.029.

[129] R. F. Egerton. *Physical principles of electron microscopy - an introduction to TEM, SEM, and AEM*. 2nd ed. Switzerland: Springer International Publishing, 2016. DOI: 10.1007/978-3-319-39877-8.

[130] W. Zhou, R. Apkarian, Z. L. Wang, and D. Joy. "Fundamentals of scanning electron microscopy (SEM)". *Scanning Microscopy for Nanotechnology: Techniques and Applications*. Ed. by W. Zhou and Z. L. Wang. New York, NY: Springer New York, 2007, pp. 1–40. DOI: 10.1007/978-0-387-39620-0_1.

[131] V. Miguel-Pérez, A. Martínez-Amesti, M. L. Nó, A. Larrañaga, and M. I. Arriortua. The effect of doping $(Mn,B)_3O_4$ materials as protective layers in different metallic interconnects for solid oxide fuel cells. *Journal of Power Sources* **243** (2013), 419–430. DOI: 10.1016/j.jpowsour.2013.05.109.

[132] S. Chevalier, G. Caboche, K. Przybylski, and T. Brylewski. Effect of nano-layered ceramic coatings on the electrical conductivity of oxide scale grown on ferritic steels. *Journal of Applied Electrochemistry* **39** (2009), 529–534. DOI: 10.1007/s10800-008-9726-9.

[133] T. Brylewski, A. Kruk, M. Bobruk, A. Adamczyk, J. Partyka, and P. Rutkowski. Structure and electrical properties of Cu-doped Mn-Co-O spinel prepared via soft chemistry and its application in intermediate-temperature solid oxide fuel cell

interconnects. *Journal of Power Sources* **333** (2016), 145–155. DOI: 10.1016/j.jpowsour.2016.09.136.

[134] Y. Xu, Z. Wen, S. Wang, and T. Wen. Cu doped Mn–Co spinel protective coating on ferritic stainless steels for SOFC interconnect applications. *Solid State Ionics* **192** (2011), 561–564. DOI: 10.1016/j.ssi.2010.05.052.

[135] B.-K. Park, J.-W. Lee, S.-B. Lee, T.-H. Lim, S.-J. Park, C.-O. Park, and R.-H. Song. Cu- and Ni-doped $Mn_{1.5}Co_{1.5}O_4$ spinel coatings on metallic interconnects for solid oxide fuel cells. *International Journal of Hydrogen Energy* **38** (2013), 12043–12050. DOI: 10.1016/j.ijhydene.2013.07.025.

[136] B. Talic, S. Molin, K. Wiik, P. V. Hendriksen, and H. L. Lein. Comparison of iron and copper doped manganese cobalt spinel oxides as protective coatings for solid oxide fuel cell interconnects. *Journal of Power Sources* **372** (2017), 145–156. DOI: 10.1016/j.jpowsour.2017.10.060.

[137] K. Lee, B. Yoon, J. Kang, S. Lee, and J. Bae. Evaluation of Ag-doped $(Mn,Co)_3O_4$ spinel as a solid oxide fuel cell metallic interconnect coating material. *International Journal of Hydrogen Energy* **42** (2017), 29511–29517. DOI: 10.1016/j.ijhydene.2017.10.017.

[138] S. N. Hosseini, M. H. Enayati, F. Karimzadeh, and A. M. Dayaghi. $LaCrO_3/CuFe_2O_4$ composite-coated Crofer 22 APU stainless steel interconnect of solid oxide fuel cells. *Metallurgical and Materials Transactions A* **48** (2017), 3490–3496. DOI: 10.1007/s11661-017-4084-z.

[139] F. Shen and K. Lu. Co_3O_4/Sm-doped CeO_2/Co_3O_4 trilayer coating on AISI 441 interconnect for solid oxide fuel cells. *ACS Applied Materials & Interfaces* **9** (2017), 6022–6029. DOI: 10.1021/acsami.6b14562.

[140] J. A. K. Tareen, A. Małecki, J. P. Doumerc, J. C. Launay, P. Dordor, M. Pouchard, and P. Hagenmuller. Growth and electrical properties of pure and Ni-doped Co_3O_4 single crystals. *Materials Research Bulletin* **19** (1984), 989–997. DOI: 10.1016/0025-5408(84)90212-5.

[141] P. Alnegren. "Corrosion of ferritic stainless steel interconnects for solid oxide cells – challenging operating conditions". Thesis. 2018.

[142] V. Bongiorno, P. Piccardo, S. Anelli, and R. Spotorno. Influence of surface finishing on high-temperature oxidation of AISI type 444 ferritic stainless steel used in SOFC stacks. *Acta Metallurgica Sinica (English Letters)* **30** (2017), 697–711. DOI: 10.1007/s40195-017-0543-1.

[143] S. Leistikow, I. Wolf, and H. J. Grabke. Effects of cold work on the oxidation behavior and carburization resistance of Alloy 800. *Materials and Corrosion* **38** (1987), 556–562. DOI: 10.1002/maco.19870381003.